remote sensing

MDPI

Article

Multipath and Deep Learning-Based Detection of Ultra-Low Moving Targets Above the Sea

Zhaolong Wang, Xiaokuan Zhang, Weike Feng *, Binfeng Zong, Tong Wang, Cheng Qi and Xixi Chen

Air Defense and Antimissile School, Air Force Engineering University, Xi'an 710051, China; wangzhaolong2022@163.com (Z.W.); ezxk@sina.com (X.Z.); zongbinfeng@163.com (B.Z.); tong_wang001@163.com (T.W.); qc_afeu@163.com (C.Q.); xixichen99@163.com (X.C.)
* Correspondence: fengweike007@163.com

Abstract: An intelligent approach is proposed and investigated in this paper for the detection of ultra-low-altitude sea-skimming moving targets for airborne pulse Doppler radar. Without suppressing interferences, the proposed method uses both target and multipath information for detection based on their distinguishable image features and deep learning (DL) techniques. First, the image features of the target, multipath, and sea clutter in the real-measured range-Doppler (RD) map are analyzed, based on which the target and multipath are defined together as the generalized target. Then, based on the composite electromagnetic scattering mechanism of the target and the ocean surface, a scattering-based echo generation model is established and validated to generate sufficient data for DL network training. Finally, the RD features of the generalized target are learned by training the DL-based target detector, such as you-only-look-once version 7 (YOLOv7) and Faster R-CNN. The detection results show the high performance of the proposed method on both simulated and real-measured data without suppressing interferences (e.g., clutter, jamming, and noise). In particular, even if the target is submerged in clutter, the target can still be detected by the proposed method based on the multipath feature.

Keywords: airborne radar; deep learning; moving target detection; multipath feature; range-Doppler map

check for updates

Citation: Wang, Z.; Zhang, X.; Feng, W.; Zong, B.; Wang, T.; Qi, C.; Chen, X. Multipath and Deep Learning-Based Detection of Ultra-Low Moving Targets Above the Sea. *Remote Sens.* **2024**, *16*, 4773. https://doi.org/10.3390/rs16244773

Andrzej Stateczny and Domenico Velotto

Received: 31 October 2024
Revised: 7 December 2024
Accepted: 19 December 2024
Published: 21 December 2024

Copyright: © 2024 by the authors. Licensee MDPI, Basel, Switzerland. This article is an open access article distributed under the terms and conditions of the Creative Commons Attribution (CC BY) license (https://creativecommons.org/licenses/by/4.0/).

1. Introduction

Sea-skimming moving target detection is of great importance for airborne pulse-Doppler (PD) radar in both civilian and military applications [1–3]. However, in complicated environments, the sea-skimming moving target is easily submerged in strong interferences, such as sea clutter, noise, multipath, and even jamming. To solve this problem, the typical approach is to reduce or remove the interferences by filtering. For example, moving target indication (MTI) or moving target detection (MTD) [4] can be used to reduce the effects of main-lobe clutter, where targets and clutter are distinguished by their different Doppler frequencies. However, the target signal may still be submerged by strong side-lobe clutter, and if the velocity of the target is relatively low, it is difficult to separate the target from the side-lobe clutter. The beamforming technique [5] can help to reduce the influence of side-lobe clutter, and the space–time adaptive processing (STAP) technique [6–9] can adaptively suppress main-lobe and side-lobe clutter from the angular and Doppler dimensions to effectively improve the detection performance of low-velocity targets. The problem is that the detection performance of these filter-based methods decreases significantly if the interference knowledge is inaccurate [10].

In recent years, with the rapid development of deep learning (DL) techniques, various intelligent methods have been proposed for radar target detection and have achieved better performance than traditional methods [2,11–15]. In particular, without the need for filtering and denoising processes, targets are detected with high detection performance by

exploiting their unique image features, such as multifractal spectrum [16], singularity power spectrum [17], scale invariant feature transform [18], histogram of oriented gradient [19], and so on. In the special case of PD radar [2,10,11], the target is automatically detected from interferences based on its range-Doppler (RD) image features. Typically, interferences such as clutter, noise, and jamming are modeled as extensions in the range and/or Doppler domain in the RD maps. And the moving target is modeled as an isolated point. However, the ultra-low-altitude moving target may have more RD image features, and these features have not been well exploited. In practice, for the ultra-low-altitude target, due to its interactions with the environment surface, the radar receives not only the echo reflected directly from the target but also the multipath echoes generated by the coupling scattering between the target and the environment surface [20,21].

Previous studies usually considered the multipath echo to be a kind of interference and believed that the presence of multipath will degrade the detection performance and the parameter estimation performance. Various multipath suppression methods have thus been proposed, such as MIMO radar waveform design [22], Brewster effect [23], high-range resolution [24], and array super-resolution techniques [25].

However, research [26] shows that both the direct return and multipath echoes of the target are coherent and that the multipath echoes contain target energy. In some cases, multipath can also be used to improve the adaptive radar target detection performance [27,28], human activity detection probability [29], indoor or urban object imaging performance [30,31], and tracking performance of low-angle sea-skimming targets [32]. However, the application of multipath information to improve the target detection performance by airborne PD radar for ultra-low-altitude sea-skimming moving targets has not been well exploited.

In addition, the DL-based target detection method relies on massive training data, which are difficult to obtain through outfield experiments. Therefore, the numerical simulation method can be more flexible in obtaining sufficient training data under different conditions. Although the traditional sea clutter simulation method can provide a statistical representation of the sea clutter by fitting the measured sea clutter data [33,34], it lacks the interaction between the radar and the sea surface, which cannot describe the echo characteristics under specific radar and environmental parameters. Therefore, using only the statistical models, as well as some typical clutter data, the existing echo generation model for airborne radar cannot meet the requirements for simulation under the specific scenario parameters and reflect the scattering mechanism between the radar, target, and sea surface.

To reflect the complex scattering mechanism between the radar and the environment, in recent years, many scholars have applied electromagnetic computations to radar echo simulation, such as the Doppler spectrum of sea clutter [35,36], SAR imaging of the ocean surface [37], and the echo simulation of a ship on a dynamic sea surface [38]. However, the existing composite electromagnetic model of targets above the sea [39] can only calculate the composite scattering within a certain range (the sea surface size is usually tens or hundreds of meters), it is difficult to simulate the echo of targets above large areas of the sea efficiently, and its sea surface scattering model provides only the overall average values of the environment, not the detailed local information. Due to the lack of the amplitude and phase information of local scattering units, this model is difficult to be used directly for the echo generation of clutter and multipath. At present, there is not an appropriate scattering-based echo model for the airborne radar detection of ultra-low-altitude targets above the sea.

Therefore, to improve the detection performance of ultra-low-altitude sea-skimming targets by the multipath and DL-based method, firstly, the multipath and the target on the RD maps are defined as the generalized target. Then, based on the composite electromagnetic scattering mechanism of the target and the ocean surface, a scattering-based echo generation model is established and validated to generate sufficient data for DL network training. At last, the features of the generalized target are learned by the DL-based detectors to improve the detection performance without suppressing the clutter and noise.

It should be note that designing DL networks is not the focus of this study. According to the experiment results, we found that the defined generalized target can indeed improve the target detection performance, and the proposed echo simulation model can indeed generate accurate training data to make the DL networks become applicable to the practice. In summary, the contributions of our work are as follows:

1. The image features of clutter, target, and multipath in the RD map are analyzed. The multipath and target in the RD map are defined as the generalized target, the features of the generalized target are learned through DL-based detectors to detect the target from the interferences, and the simulation results demonstrate the high detection performance of the proposed method.
2. The composite scattering model for the airborne radar detecting ultra-low-altitude targets is established. The accuracy and efficiency of the model are verified by comparing the simulation results with the accurate numerical algorithm.
3. A scattering-based echo generation model is established to generate sufficient training data, and the effectiveness of the model is verified by the comparison with real-measured data. The existence of the multipath is proven by our simulation results.

The rest of the paper is structured as follows. Section 2 describes the geometry model and the signal model. Section 3 describes the image features in RD maps, the generalized target detection by the DL-based method, and the scattering-based echo generation model in detail. Section 4 describes the target detection results of the DL-based method. Finally, the conclusions are given in Section 5.

2. Geometry Model and Signal Model

This section presents the geometry and signal models for the airborne radar detection of ultra-low-altitude sea-skimming targets. Based on these, the RD maps are generated.

The geometry model of the airborne radar detecting sea-skimming ultra-low-altitude targets is shown in Figure 1, where the radar center position vector is $\boldsymbol{P}_S = [S_x, S_y, S_z]$, the radar velocity vector is $\boldsymbol{V}_r = [v_{rx}, v_{ry}, v_{rz}]$, the target center position vector is $\boldsymbol{P}_T = [T_x, T_y, T_z]$, the target velocity vector is $\boldsymbol{V}_t = [v_{tx}, v_{ty}, v_{tz}]$, and the direction along the coordinate axis is the positive direction.

For the linear frequency modulation (LFM) pulse radar, the transmit signal can be written as

$$s_t(t) = \mathrm{rect}\left(\frac{t}{T_p}\right) e^{\mathrm{j}2\pi\left(f_0 t + K_r t^2/2\right)} \tag{1}$$

where rect(·) is a rectangular function, f_0 represents the carrier frequency, $Kr = B_W/T_p$ donates the linear frequency modulation rate, B_W is the signal bandwidth, and T_p is the pulse width.

The echo response of each scattering unit received by the radar at time t can be expressed as

$$S'(t) = A\gamma s_t(t-\tau) e^{\mathrm{j}2\pi f_d(t-\tau)} \tag{2}$$

where $A = ((\lambda^2 G_i G_r)/((4\pi)^3 R_i^2 R_r^2))^{1/2}$, where G_i and G_r represent the transmitting antenna gain and the receiving antenna gain, respectively, and R_i and R_r represent the distance from the scattering unit to the transmitting antenna and receiving antenna, respectively; $\gamma = \sigma^{1/2} e^{\mathrm{j}\phi}$, where σ is the radar cross section (RCS) of the scattering unit and ϕ is a phase term when electromagnetic scattering occurs on the scattering unit; τ represents the time delay from transmission to reception of the electromagnetic wave; and f_d represents the Doppler frequency.

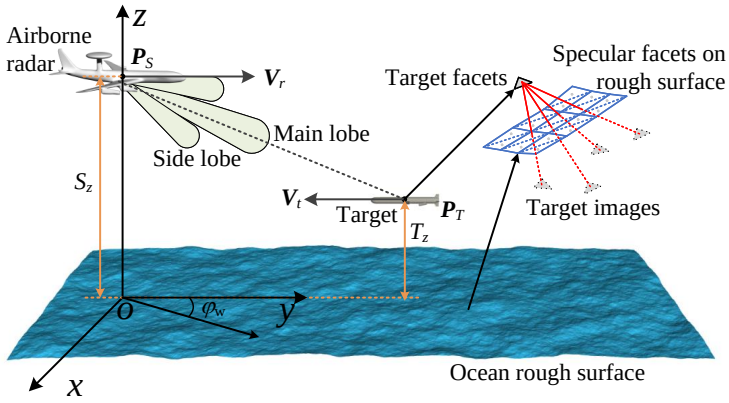


Figure 1. The geometry model of the airborne radar detecting sea-skimming ultra-low-altitude targets.

After zero intermediate frequency (zero-IF) processing for $S'(t)$, the baseband signal $S_r(t)$ can be expressed as

$$S_r(\boldsymbol{t}_f, \boldsymbol{t}_s) = A(\boldsymbol{t}_s)\gamma\text{rect}\left(\frac{t'(\boldsymbol{t}_f, \boldsymbol{t}_s)}{T_p}\right)\varphi(t'(\boldsymbol{t}_f, \boldsymbol{t}_s))e^{\text{j}2\pi f_d(t'(\boldsymbol{t}_f, \boldsymbol{t}_s))} \tag{3}$$

where $t'(\boldsymbol{t}_f, \boldsymbol{t}_s) = \boldsymbol{t}_f - (R_i(\boldsymbol{t}_s) + R_r(\boldsymbol{t}_s))/c$, $\boldsymbol{t}_f$ denotes the fast time vector, and $\boldsymbol{t}_s$ represents the slow time vector, $\varphi(t) = e^{j\pi K_r t^2}$. Considering all the possible components, the total received echo can be written as follows:

$$X(\boldsymbol{t}_f, \boldsymbol{t}_s) = S(\boldsymbol{t}_f, \boldsymbol{t}_s) + J(\boldsymbol{t}_f, \boldsymbol{t}_s) + N(\boldsymbol{t}_f, \boldsymbol{t}_s) \tag{4}$$

where $J(\boldsymbol{t}_f, \boldsymbol{t}_s)$ and $N(\boldsymbol{t}_f, \boldsymbol{t}_s)$ denote the jamming and noise signals, respectively, and $S(\boldsymbol{t}_f, \boldsymbol{t}_s)$ represents the echo of the total scattering units, which can be written as

$$S(\boldsymbol{t}_f, \boldsymbol{t}_s) = \sum_N S_r(\boldsymbol{t}_f, \boldsymbol{t}_s) \tag{5}$$

where N denotes the number of target and environmental scattering units in the echo response.

The two-dimensional (2D) RD maps can be obtained by PD processing of the received echoes. Firstly, the pulse compression is adopted by using the matched filtering method in the fast time domain (range dimension), and $X_{pc}(\boldsymbol{r}, \boldsymbol{t}_s)$ is set as the result after pulse compression, which can be expressed as

$$X_{pc}(\boldsymbol{r}, \boldsymbol{t}_s) = IFFT\Big\{FFT[X(\boldsymbol{t}_f, \boldsymbol{t}_s) \otimes h(\boldsymbol{t}_f)]\Big\} \tag{6}$$

where $h(\boldsymbol{t}_f)$ represents the transfer function of the matched filter, and $\otimes$ represents the convolution. FFT represents the fast Fourier transform, and $IFFT$ represents the inverse FFT.

Then, the Fourier transform is conducted in the slow-time domain (Doppler dimension) for the frequency domain filtering, and the result can be expressed as

$$X_{RD}(\boldsymbol{r}, \boldsymbol{f}_d) = FFT\{X_{pc}(\boldsymbol{r}, \boldsymbol{t}_s)\} \tag{7}$$

where $\boldsymbol{f}_d$ represents the Doppler frequency vector.

Finally, the RD maps are generated after normalization and threshold filtering, which can be expressed as

$$\bar{X}_{RD} = \frac{|X_{RD}| - \min\{|X_{RD}|\}}{\max\{|X_{RD}|\} - \min\{|X_{RD}|\}} \tag{8}$$

$$X_{nor} = \bar{X}_{RD}\frac{\max\{\bar{X}_{RD} - \eta, 0\}}{\bar{X}_{RD} - \eta} \tag{9}$$

where $|\cdot|$ and $\max\{\cdot\}$ indicate taking the absolute and maximum values, respectively, and η is the threshold value.

3. Generalized Target Detection via DL-Based Method

As shown in Figure 2, the generalized target detection via the DL-based method is proposed in this section, where the RD map features in the real-measured data are analyzed, and the generalized target is defined in Section 3.1; then in Section 3.2, the DL-based moving target detection method is proposed, and the features of the generalized target are learned through DL-based detectors; finally, in Section 3.3, the composite scattering model and the scattering-based echo generation model are established to generate sufficient data for DL-based network training, and the effectiveness of the echo generation model is verified by the comparison with real-measured data.

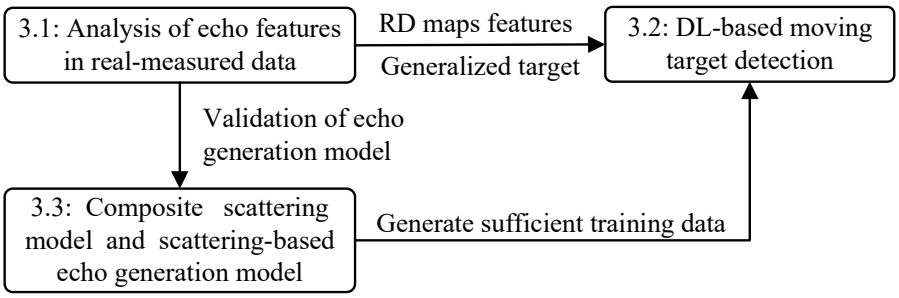


Figure 2. The proposed generalized target detection via the DL-based method.

3.1. Analysis of Echo Features in Real-Measured Data

The real-experiment scenario is shown in Figure 3, where the radar carrier and the target are both Cessna 208 aircraft, the height of the carrier and target are S_Z = 1.2 km and T_Z = 100 m, respectively, and the two aircraft are flying in opposite directions at a velocity of 110 m/s.

The RD map of the real-measured data is shown in Figure 4, where the slant distance between the carrier and the target is R_t = 5.3 km. From Figure 4, it can be seen that there is an obvious RD image feature of each component:

(1) The clutter obeys a curve and vertical line image feature, and there is a strong altitude line clutter at the Doppler frequency of 0 Hz. At the same time, the jamming, with a vertical line image feature, is also distributed in the range dimension at the 0 Hz Doppler frequency.
(2) The target and multipath echoes have a point-like feature, where the multipath echoes, as parts of the target echo, are distributed in both the range and Doppler dimensions and are larger than the target echo in the range dimension and smaller than the target echo in the Doppler dimension.
(3) The target echo is also distributed in the Doppler dimension due to the micro-motion of the blades.

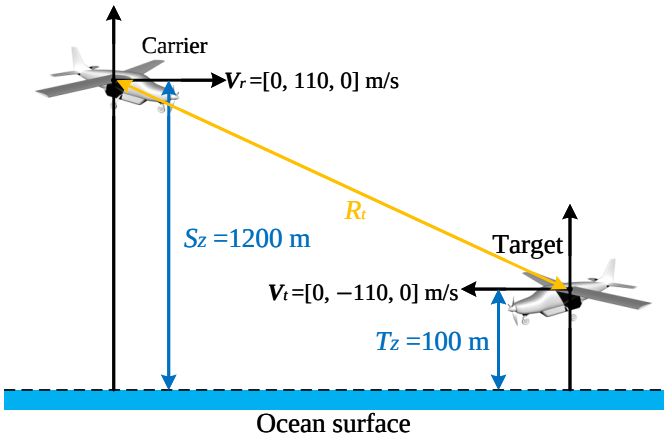


Figure 3. The real-experiment scenario.

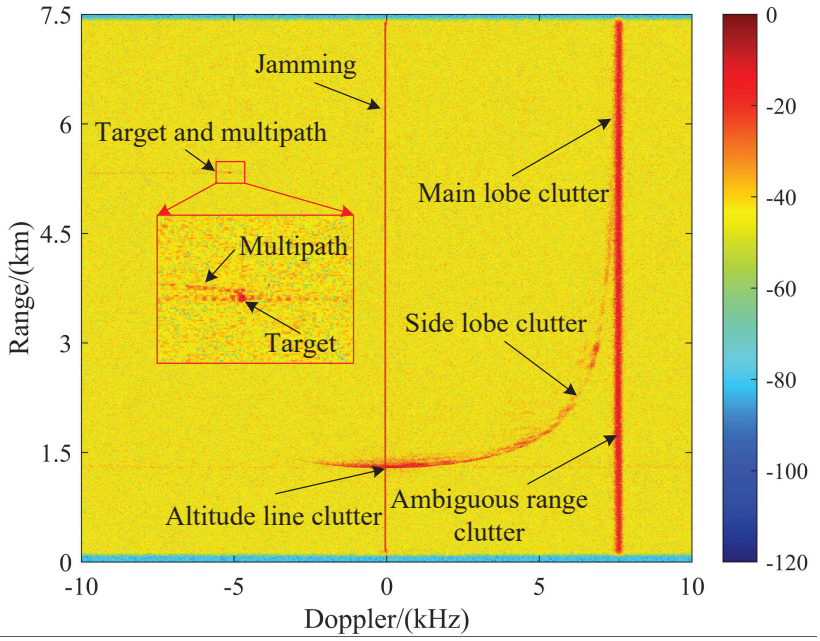


Figure 4. The RD map of the real-measured data.

In conventional methods, the moving target is modeled as an isolated point on the RD map. However, from the real-measured RD map shown in Figure 4, there is a multipath around the echo of ultra-low-altitude targets. Based on the target-like feature of the multipath, in this study, the multipath and the target are defined together as a generalized target with the unique RD image feature. The detection performance based on DL-based algorithms used for ultra-low-altitude targets is analyzed in the following sections.

3.2. DL-Based Moving Target Detection

As shown in Figure 5, in the existing constant false alarm detection (CFAR)-based moving target detection method, the interference suppression is performed during Doppler processing after matched filtering the received radar echoes, and then the CFAR detector is used for target detection.

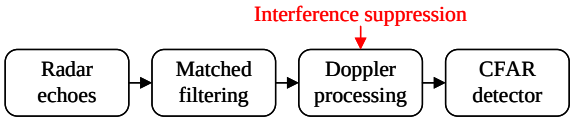


Figure 5. Existing CFAR-based moving target detection method.

Instead of suppressing the interference, the DL-based method in this paper detects the target directly by learning the target features in RD maps without suppressing the interference as shown in Figure 6.

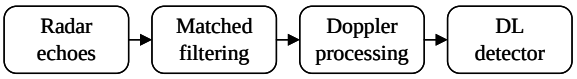


Figure 6. DL-based moving target detection method.

At present, the mainstream DL-based target detection algorithms are divided into two categories: single-stage detectors, such as YOLO series and SSD series, and two-stage detectors, such as RCNN, Fast R-CNN, Faster R-CNN, FPN, etc. In this study, YOLOv7 [40] and Faster R-CNN [41] are applied to illustrate the detection performance of learning the generalized target features.

3.2.1. YOLOv7 Algorithm

YOLOv7 [40] is one of the latest achievements in one-stage object detection algorithms, with improved detection efficiency and accuracy compared to previous algorithms. The architecture of basic YOLOv7 consists of four main components: input, backbone, neck, and head.

Input: The input network preprocesses the input images, mainly including Mosaic data enhancement, adaptive image scaling, and adaptive anchor frame calculation.

Backbone: The backbone network mainly includes the Convolutional-Batch Normalization-SiLU (CBS) module, the efficient layer aggregation network (ELAN) module, and the Max Pooling (MP) module, and its main function is feature extraction.

Neck: The neck network also consists of the CBS, ELAN, and MP modules. Different from the backbone network, there are two upsample modules. The main function of upsampling is to improve feature extraction using PANet [42]. In addition, the neck network also contains the SPPCSPC module, which can significantly improve the receptive field and feature expression capability.

Head: The head network uses the RepConv module to adjust the number of channels and uses 1 × 1 convolution operations to predict the target confidence, category, and regression detection box.

3.2.2. Faster R-CNN

Faster R-CNN is a typical representative of the two-stage target detector [41]. The basic framework of Faster R-CNN consists of three main parts: Convolution layer (conv layers), Region Proposal Network (RPN), region of interest pooling (RoIPooling) and Classifier.

Conv layers: Conv layers is a feature extraction network for resized input images. Vgg-16 is selected for feature extraction in this paper, and the Conv layers are composed of 13 conv layers, 13 Relu layers, and 4 pooling layers.

RPN: The RPN slides windows on the feature map to generate region proposals, anchors the candidate regions with boxes, and predicts whether the boxes contain objects.

RoIPooling and Classifier: This network classifies the candidate boxes and fine-tunes the coordinates of the candidate boxes. Finally, it outputs the regression and box classification information.

3.3. Scattering-Based Echo Generation Model

The DL-based target detection method relies on massive training data. However, due to the single parameter change of the outfield experiment scenario, the data obtained only through real experiments are relatively limited. Therefore, a scattering-based echo generation model is established to obtain accurate and sufficient training data for DL network training and to reflect the complex scattering mechanism of ultra-low-altitude target detection by airborne radar.

3.3.1. The Composite Scattering Model

As can be seen from Figure 1, when the radar irradiates the ultra-low-altitude target, the echo received by the radar includes not only the direct scattering from the target but also environmental scattering (clutter) and higher-order coupling responses between the target and the ocean surface (multipath scattering). Existing composite electromagnetic models of targets above the sea [39] can only calculate the composite scattering within a certain range, as it is difficult to simulate the echo of targets above large areas of the sea efficiently. Therefore, it is necessary to establish an appropriate electromagnetic model for each scattering component. In this section, the composite scattering model of airborne radar detecting ultra-low-altitude target is proposed, where the establishment of the ocean surface scattering model, the target, and multipath scattering model is shown in subsections 'Ocean Surface Scattering Model' to 'Target and Multipath Scattering Model', respectively.

Ocean Surface Scattering Model

Electromagnetic scattering from the ocean surface is the source of clutter. The sea surface scattering model in [39] (the two-scale model method) provides only the overall scattering characteristics of the environment; its simulated results are average values, not the detailed local information. However, limited by the range resolution and azimuth interval of the airborne radar, the local scattering information of each scattering unit is equally important for echo generation, e.g., the local scattering amplitude and phase. The facet-based two-scale model (FBTSM) algorithm is proposed to calculate the local scattering of the large-scale ocean surface in an arbitrary region.

The ocean surface is usually modeled as a random fluctuation model with statistical properties and can be generated as a rough surface via Monte Carlo methods [43] with a given spectrum. (In this study, the Elfouhaily spectrum [44] is used for modeling, the positive direction of wind speed is along the y-axis, and the angle between the wind direction and the y-axis is φ_{w} as shown in Figure 1). The entire rough surface is then meshed into triangular facets of a given size, the principles of facet meshing are described in detail in [45].

The normalization radar cross section (NRCS) of the ocean rough surface calculated by the proposed FBTSM algorithm can be expressed as

$$\sigma_{hv}^{total}\left(\hat{\boldsymbol{k}}_{\mathrm{i}},\hat{\boldsymbol{k}}_{\mathrm{s}}\right)=\frac{1}{A'}\cdot\sum_{n=1}^{N'}\left\{\left[\sigma_{hv}^{\mathrm{KAM}}(\hat{\boldsymbol{k}}_{\mathrm{i}},\hat{\boldsymbol{k}}_{\mathrm{s}})_n+\sigma_{hv}^{\mathrm{SPM}}(\hat{\boldsymbol{k}}_{\mathrm{i}},\hat{\boldsymbol{k}}_{\mathrm{s}})_n\right]\Delta S_n\right\} \tag{10}$$

where $\hat{\boldsymbol{k}}_{\mathrm{i}}$ and $\hat{\boldsymbol{k}}_{\mathrm{s}}$ represent the unit vector along the incident and scattering directions, the subscripts v and h represent the vertical and horizontal polarizations, N' represents the total number of ocean surface facets, and A' represents the area of the total rough surface. ΔS_n represents the area of each facet. The meaning of other variables and the specific derivations to get (10) can be found in Appendix A.1.

In the radar irradiation area, the clutter region cannot be considered a single scatter. As shown in Figure 7, the entire clutter region is divided into multiple range-Doppler cells [46]. The scattering amplitude and Doppler frequency at the center of the cell represent

that of the entire cell. Δr is the width of the range cell, which is determined by the range resolution, which can be written as

$$\Delta r \approx \Delta R \sec \varphi = \frac{c}{2B_W} \sec \varphi \tag{11}$$

where ΔR is the radar range resolution, c is the EM wave velocity, B_W is the signal bandwidth, and φ donates the grazing angle of the scattering unit. The azimuth interval $\Delta\theta$ of the range-Doppler cell can be expressed as

$$\Delta\theta \approx \frac{\lambda f_r}{4Kv_r \cos\varphi} \tag{12}$$

where λ represents the EM wavelength, f_r represents the pulse repetition frequency (PRF), K is the number of pulses in a coherent processing interval (CPI), and v_r is the velocity of the radar. After Δr and $\Delta\theta$ are obtained, the area of the range-Doppler cell ΔS is obtained by $\Delta S = R \cdot \Delta r \cdot \Delta\theta$, where R represents the range from the radar to the scattering center. Then, according to (10), the RCS of the range-Doppler cell σ_c can be obtained by $\sigma_c = \Delta S \cdot \sigma_{hv}^{total}$.

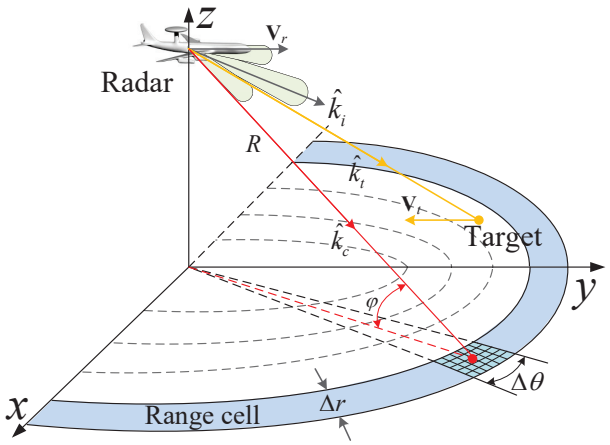


Figure 7. Schematic diagram of the range-Doppler cells.

Target and Multipath Scattering Model

The multipath scattering of ultra-low-altitude targets is essentially the coupling scattering between the target and the ocean surface. Figure 8a shows several simple ray tracing paths, and the shooting and bouncing ray (SBR) method [39,47] is used to describe the interactions between target facets and ocean surface facets.

As shown in Figure 8b, the direction and amplitude of the rays are traced based on the geometric optics (GO) method, where the i-th reflected field vector can be calculated from the i-th incident field vector at each reflection point, and the i-th reflected field is used as the $(i+1)$-th incident field. The specific derivations of the i-th reflection on a triangular facet based on the GO method can be found in Appendix A.2.

The far-field scattering of the facets is calculated after the completion of ray tracing. If the final facet is on the ocean surface, the scattering is calculated by the FBTSM method in Section 3.3.1. For the scattering of the target facets, the far-field scattering is calculated by the physical optics (PO) method, which is given by

$$\boldsymbol{E}_{PO}^{\mathrm{s}} \approx \frac{\mathrm{j}k_0}{4\pi} \frac{e^{-\mathrm{j}k_0 r}}{r} \cdot \left[\hat{\boldsymbol{k}}_{\mathrm{s}} \times (\hat{\boldsymbol{M}}_{\mathrm{s}}(\hat{r}') + \eta_0 \hat{\boldsymbol{k}}_{\mathrm{s}} \times \hat{\boldsymbol{J}}_{\mathrm{s}}(\hat{r}'))\right] \Delta \mathrm{A}_n I \tag{13}$$

$$I = \frac{1}{\Delta A_n} \int_{S_n} e^{\left[-\mathrm{j}k_0(\hat{\boldsymbol{k}}_{\mathrm{i}} - \hat{\boldsymbol{k}}_{\mathrm{s}}) \cdot \hat{r}'\right]} \mathrm{d}S' \tag{14}$$

where j represents the imaginary unit, k_0 represents the EM wave number in free space, η_0 represents the wave impedance in free space, r represents the far-field distance, and $\hat{r}'$ is the last facet position vector. The integral in (14) can be solved by Gordon's method [48]. The facet mesh size is 1/10 incident wavelength. $\hat{\boldsymbol{J}}_s(\hat{r}')$ and $\hat{\boldsymbol{M}}_s(\hat{r}')$ are the electric and magnetic currents on the illuminated facet, which can be expressed as follows:

$$\hat{\boldsymbol{J}}_s(\hat{r}') = \hat{\boldsymbol{n}} \times (\hat{\boldsymbol{E}}_i(\hat{r}') + \hat{\boldsymbol{E}}_r(\hat{r}')) \tag{15}$$

$$\hat{\boldsymbol{M}}_s(\hat{r}') = -\hat{\boldsymbol{n}} \times (\hat{H}_i(\hat{\boldsymbol{r}}') + \hat{\boldsymbol{H}}_r(\hat{r}')) \tag{16}$$

where $\hat{\boldsymbol{E}}_{i/r}(\hat{r}')$ and $\hat{\boldsymbol{H}}_{i/r}(\hat{r}')$ represent the incident or reflected electric and magnetic fields, respectively.

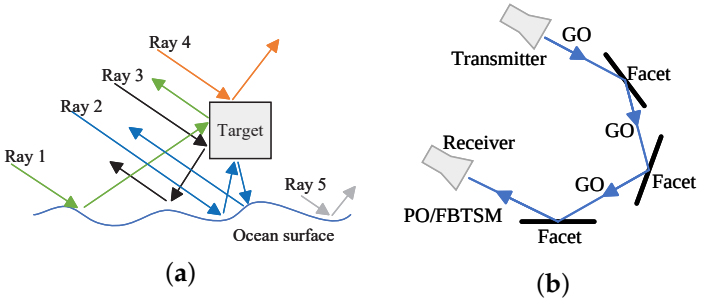


Figure 8. SBR method based on ray tracing. (**a**) Multiple scattering between the sea surface and the target. (**b**) Schematic diagram of a certain ray.

3.3.2. Echo Generation Model

The echo generation can be performed after the scattering calculations for each component have been completed. Taking into account all the possible scattering components for $S(\boldsymbol{t}_f, \boldsymbol{t}_s)$ in (4), $S(\boldsymbol{t}_f, \boldsymbol{t}_s)$ can be written as

$$S(\boldsymbol{t}_f, \boldsymbol{t}_s) = T(\boldsymbol{t}_f, \boldsymbol{t}_s) + C(\boldsymbol{t}_f, \boldsymbol{t}_s) + M(\boldsymbol{t}_f, \boldsymbol{t}_s) \tag{17}$$

where $T(\boldsymbol{t}_f, \boldsymbol{t}_s)$, $C(\boldsymbol{t}_f, \boldsymbol{t}_s)$, and $M(\boldsymbol{t}_f, \boldsymbol{t}_s)$ represent the echo of target, clutter, and multipath, respectively.

For the target echo, $T(\boldsymbol{t}_f, \boldsymbol{t}_s)$ can be expressed as

$$T(\boldsymbol{t}_f, \boldsymbol{t}_s) = \sum_{N_t} \left(A(\boldsymbol{t}_s)\gamma_t \mathrm{rect}\left(\frac{t'(\boldsymbol{t}_f, \boldsymbol{t}_s)}{T_p} \right) \varphi(t'(\boldsymbol{t}_f, \boldsymbol{t}_s)) e^{\mathrm{j}2\pi f_{dt}(t'(\boldsymbol{t}_f, \boldsymbol{t}_s))} \right) \tag{18}$$

$$f_{dt} = 2(V_r - V_t) \cdot \hat{k}_t / \lambda \tag{19}$$

where N_t represents the number of scattering facets of the target. γ_t is calculated by the PO method in subsection 'Target and Multipath Scattering Model'. $\hat{k}_t$ is the unit vector from the radar to the center of the target facets.

For the clutter echo, $C(\boldsymbol{t}_f, \boldsymbol{t}_s)$ can be expressed as

$$C(\boldsymbol{t}_f, \boldsymbol{t}_s) = \sum_{N_c} \left(A(t_s)\gamma_c \mathrm{rect}\left(\frac{t'(\boldsymbol{t}_f, \boldsymbol{t}_s)}{T_p} \right) \varphi(t'(\boldsymbol{t}_f, \boldsymbol{t}_s)) e^{\mathrm{j}2\pi f_{dct}(t'(\boldsymbol{t}_f, \boldsymbol{t}_s))} \right) \tag{20}$$

$$f_{dct} = 2V_r \cdot \hat{k}_c / \lambda \tag{21}$$

where N_c represents the number of range-Doppler cells. $\hat{k}_c$ is the unit vector from the radar to the center of the range-Doppler cell. γ_c is calculated by the FBTSM method in subsection 'Ocean Surface Scattering Model'.

For the multipath echo, $M(\boldsymbol{t}_f, \boldsymbol{t}_s)$ can be expressed as

$$M(\boldsymbol{t}_f, \boldsymbol{t}_s) = \sum_{N_m} \left(A(\boldsymbol{t}_s)\gamma_m \text{rect}\left(\frac{\boldsymbol{t}_f - R_{mn}(\boldsymbol{t}_s)/c}{T_p} \right) \varphi(\boldsymbol{t}_f - \frac{R_{mn}(\boldsymbol{t}_s)}{c}) e^{\text{j}2\pi f_{dmt}(\boldsymbol{t}_f - \frac{R_{mn}(\boldsymbol{t}_s)}{c})} \right) \tag{22}$$

where N_m represents the number of total rays during ray tracing. R_{mn} is the total path length of each ray from emission to reception. γ_m is calculated by the SBR method in Section 3.3.2. It should be noted that in the simulation of multipath echoes, as shown in Figure 9, the Doppler frequency f_{dmt} in multipath echoes can be represented as

$$f_{dmt} = \frac{(V_r - V_1) \cdot \hat{\boldsymbol{k}}_1}{\lambda} + \sum_{i=2}^{n} \frac{(V_{i-1} - V_i) \cdot \hat{\boldsymbol{k}}_{n-1}}{\lambda} + \frac{(V_n - V_r) \cdot \hat{\boldsymbol{k}}_n}{\lambda} \tag{23}$$

Finally, (17)–(23) are brought into (4), and the simulated 2D RD maps can be obtained by the PD processing shown in Section 2. To simplify the simulation model, the echo of noise and $N(\boldsymbol{t}_f, \boldsymbol{t}_s)$ in (4) is modeled as additive complex Gaussian white noise with a specific signal-to-noise ratio (SNR), and there is no additional jamming $J(\boldsymbol{t}_f, \boldsymbol{t}_s)$ in the simulation process to generate the training data.

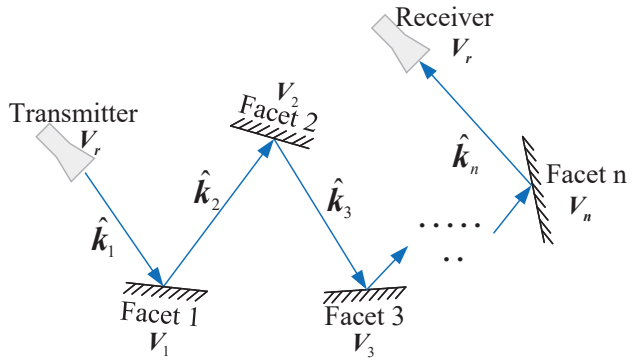


Figure 9. Doppler shift in the multipath scattering.

4. Model Validation and Experiment Analysis

This section focuses on validating the developed models and analyzing the detection results. Section 4.1 shows the validation of the scattering model and the scattering-based echo generation model. Section 4.2 presents the multipath echo features and the existence of the multipath echo. At last, the detection performance of the generalized target is analyzed in Section 4.3.

4.1. Model Validation

4.1.1. Validation of the Scattering Model

To validate the accuracy of the SBR-FBTSM, the mono-static composite scattering of a target above the ocean rough surface is calculated by the proposed SBR-FBTSM and the exact numerical solver, the multi-level fast multipole algorithm (MLFMA). The frequency of the incident wave is 10G Hz, the size of the rough surface is 100 × 100 m, the wind speed 10 m above the sea surface is v_{10} = 5 m/s, the angle between the wind direction and the y-axis is φ_w = 0°, the dielectric constant of the rough surface is ε_r = (56.1865, 37.4300) from the Debye model [49], and the target, located at T_Z = 25 m in height, is a perfect electric conductor (PEC) missile-like target with a length of 5.56 m. The incident angle is set as $\theta_i = 0°\sim90°$, $\varphi_i = 0°$. The scattering result is averaged 30 times in Monte Carlo simulations. Our simulations are executed on a personal computer with an Intel(R) Xeon(R) Gold 5218 2.3 GHz CPU and 64 G RAM. Programs are built and run under the Windows 11 64-bit operating system. Figure 10 shows the mono-static composite radar cross section (RCS) of the target above a rough sea surface under different polarizations, where RCS-T represents the target RCS, RCS-M represents the multipath RCS, RCS-S is the RCS of the

rough surface, and RCS-SBR-FBTSM and RCS-MLFMA represent the total RCS calculated by SBR-FBTSM and MLFMA, respectively.

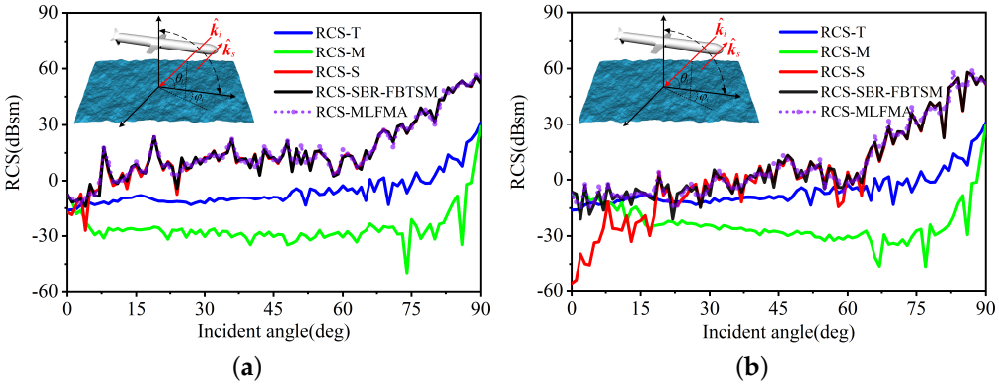


Figure 10. Comparisons of the mono-static composite scattering of the target above a rough sea surface. (**a**) Vertical–vertical (VV) polarization. (**b**) Horizontal–horizontal (HH) polarization.

As shown in Figure 10, the results of the SBR-FBTSM agree well with the results of the MLFMA, and the computation times of SBR-FBTSM under VV-polarization and HH-polarization are 1139.35 s and 1136.22 s, respectively. The computation times of MLFMA under two polarizations are 21,460.35 s and 21,448.34 s, respectively. Therefore, the SBR-FBTSM proposed in this study can simulate the composite scattering between large sea areas and targets more efficiently than the exact numerical solver.

4.1.2. Validation of the Scattering-Based Echo Generation Model

To verify the accuracy of the echo model, this section compares the RD maps obtained from the proposed echo generation model with the real-measured data. The parameters are set as v_{10} = 1.2 m/s, φ_w = 0°, ε_r = (56.1865, 37.4300), f_0 = 10 GHz, B_W = 80 MHz, $T_p = 2 \times 10^{-7}$ s, f_r = 20 kHz, K = 512, the incidence and reception of airborne radar are both VV polarization, the radar uses a two-dimensional array antenna with 64 × 64 elements, the radar main lobe is aligned with the target, the radar side lobe gain is −15 dB, and the maximum range of clutter is 15 km. Figure 11 shows the RD map when the slant distance between the carrier and the target is R_t = 5.3 km of the simulation data.

It can be seen from Figure 11 that the variation trends of main lobe clutter, side lobe clutter, altitude line clutter, target echo, and multipath echo in the simulation RD map are consistent with those of the same components in the real-measured RD map in Figure 4.

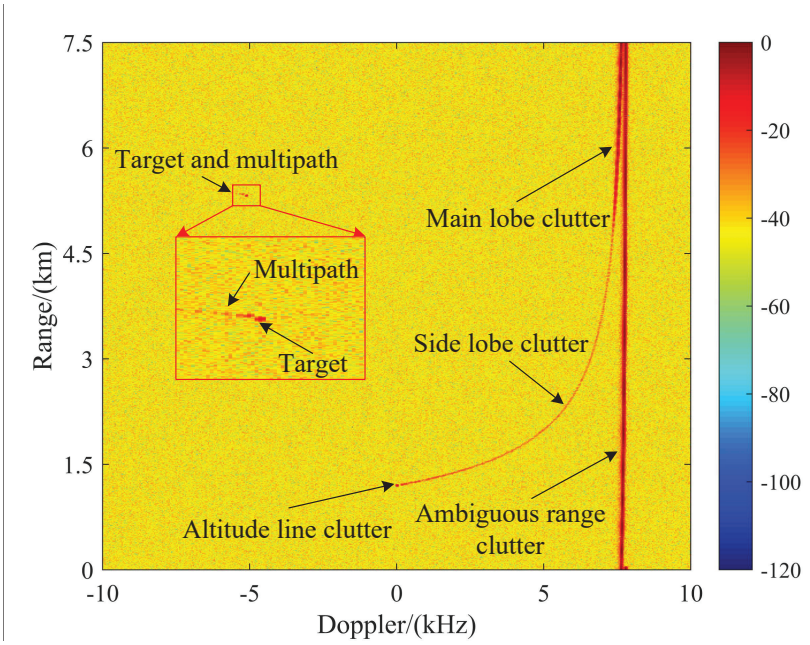


Figure 11. The RD map of the simulation data.

It should be noted that as the Cessna 208 has blades, the target echo is also distributed in the Doppler dimension in the real-measured RD map in Figure 4. However, since ultra-low-altitude targets such as missiles, fixed-wing UAVs and fighters do not have a significant blade, the micro-motion feature of the blades is not considered in the simulated RD maps. At the same time, the jamming, with a vertical-line image feature at the 0 Hz Doppler frequency, is also not considered.

4.2. Multipath Echo Characteristics and the Existence of the Multipath Echo

Figure 12 shows the echo of the ultra-low-altitude target under different parameters on the RD maps, where the length and width of the PEC fighter target are 19 m and 14 m, respectively, the length and width of the PEC fixed-wing UAV are 11 m and 20 m, respectively, f_0 = 10G Hz, f_r = 100k Hz, K = 512, ε_r = (56.1865, 37.4300), $T_p = 2 \times 10^{-7}$ s, P_S = [0, 0, 300] m, V_r = [0, 400, 0] m/s, T_x = 10 m, T_y = 1000 m, $v_{tx} = v_{tz}$ = 0 m/s, the incidence and reception of the airborne radar are both VV polarization, the radar uses a two-dimensional array antenna with 64 × 64 elements, the radar main lobe is aligned with the target, the radar side lobe gain is −15 dB, and the maximum range of clutter is 3000 m. Other simulation parameters are shown in Table 1. The transforming equation between velocity and Doppler frequency is $v = 0.5 \cdot c \cdot f_d / f_0$. It should be stated that, as the NRCS of the sea surface is mainly affected by wind speed and the wind direction has little effect on it [45], this study only considers the influence of wind speed on the RD image features.

(1) From Figure 12a–c, it can be seen that the received power of the altitude line clutter decreases as the wind speed v_{10} increases, while the power of the main lobe clutter increases. For multipath echoes, as the wind speed v_{10} increases, the multipath echoes broaden in the frequency dimension, and the maximum power of the multipath echoes decreases. This is because as the wind speed v_{10} increases, the ocean surface becomes rougher, the backscattering of the surface increases, and the specular scattering decreases, resulting in a decrease in the altitude line clutter and an increase in the main lobe clutter. The multipath echoes are generated by the coupling between the target and the sea surface. The higher the sea state, the more specular the scattering units of the sea surface are, resulting in a broadening of the multipath echoes in the frequency domain. The weakening of the specular scattering at the sea surface leads to a reduction in the received multipath echoes.

Table 1. Echo simulation parameters.

Number	Wind Speed (m/s)	Target Height (m)	Target Type	Target Velocity (m/s)	Signal Bandwidth (Hz)	Noise (dB)
(a)	v_{10} = **3**	T_z = 50	Missile	v_{ty} = 250	B_W = 20M	SNR = 10
(b)	v_{10} = 5	T_z = 50	Missile	v_{ty} = 250	B_W = 20M	SNR = 10
(c)	v_{10} = **8**	T_z = 50	Missile	v_{ty} = 250	B_W = 20M	SNR = 10
(d)	v_{10} = 5	T_z = **30**	Missile	v_{ty} = 250	B_W = 20M	SNR = 10
(e)	v_{10} = 5	T_z = **15**	Missile	v_{ty} = 250	B_W = 20M	SNR = 10
(f)	v_{10} = 5	T_z = 50	Missile	v_{ty} = **−250**	B_W = 20M	SNR = 10
(g)	v_{10} = 5	T_z = 50	Missile	v_{ty} = **0**	B_W = 20M	SNR = 10
(h)	v_{10} = 5	T_z = 50	**UAV**	v_{ty} = 250	B_W = 20M	SNR = 10
(i)	v_{10} = 5	T_z = 50	**Fighter**	v_{ty} = 250	B_W = 20M	SNR = 10
(j)	v_{10} = 5	T_z = 50	Missile	v_{ty} = 250	B_W = **10**M	SNR = 10
(k)	v_{10} = 5	T_z = 50	Missile	v_{ty} = 250	B_W = 20M	SNR = **20**
(l)	v_{10} = 5	T_z = 50	Missile	v_{ty} = 250	B_W = 20M	SNR = **0**

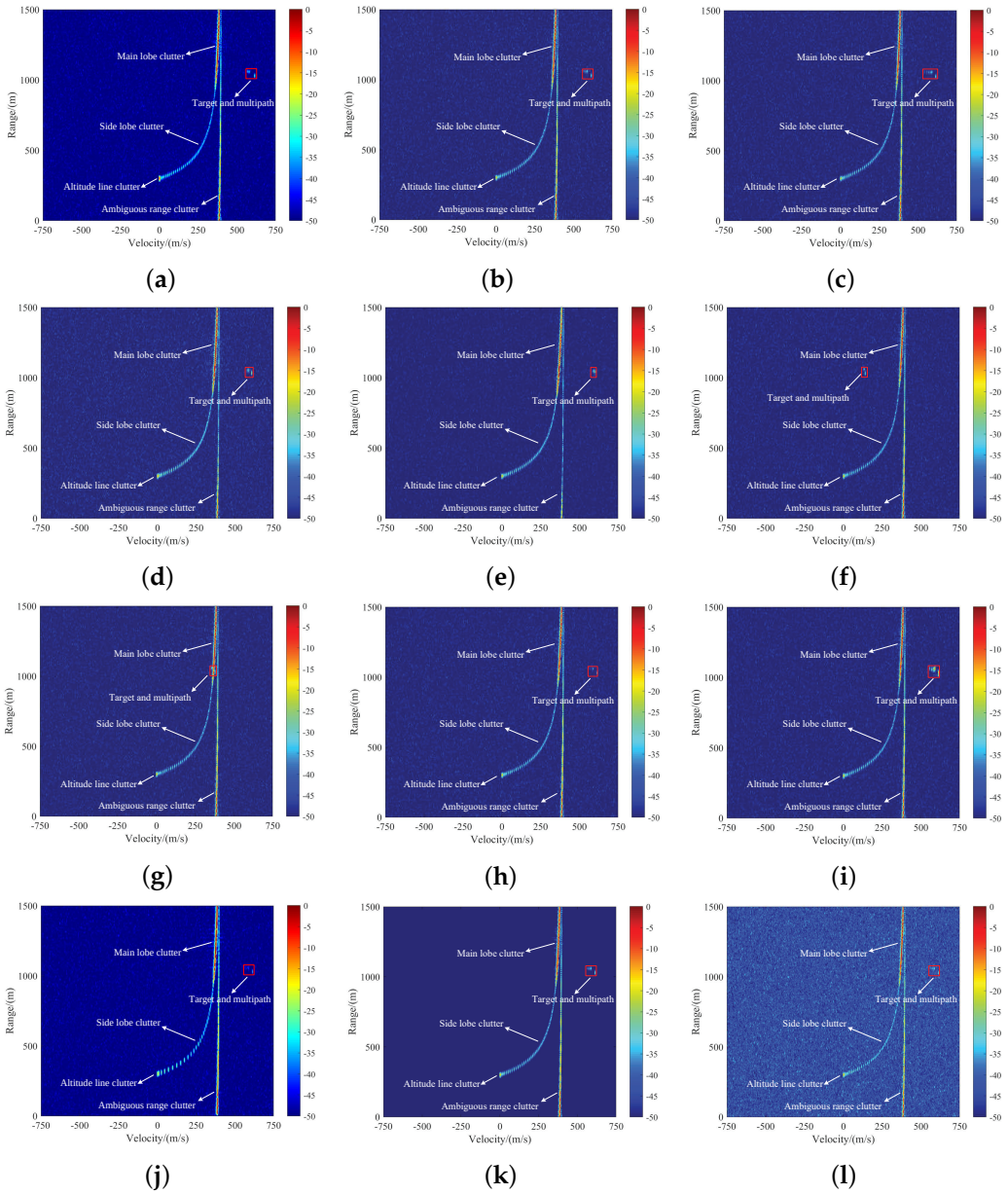


Figure 12. The RD maps of ultra-low-altitude targets under different parameters.

(2) As observed in Figure 12b,d,e, with the target height decrease, the altitude line clutter increases slightly. Meanwhile, the distribution of multipath echoes in the Doppler

dimension decreases, and the maximum power of the multipath echoes increases. The reason is that as the target height decreases, the radar main lobe points towards the target, which increases the gain in the direction directly below the radar, resulting in an increase in the altitude line clutter. At the same time, as the target height decreases, the number of specular scattering units on the ocean surface decreases, resulting in a decrease in the multipath echo distribution in the frequency dimension. The coupling scattering between the target and the sea surface increases as the height decreases, increasing the maximum power of the multipath echoes.

(3) Figure 12b,f,g show the RD maps under three conditions: radar and target head-on, target side-flying, and radar pursuing target. The figures show that when the target velocity is slow, the target echo will be submerged in clutter, making it difficult to detect the target in the RD maps.

(4) Figure 12b,h,i provide the RD maps of different targets. As can be observed, the stronger the scattering of the target, the stronger the multipath echo.

(5) Figure 12b,j plot the RD maps under different bandwidths. It can be seen that the larger the bandwidth, the greater the power of the target and multipath echoes. This is because as the bandwidth increases, the size of the clutter resolution units decreases, resulting in a decrease in clutter power and a relative increase in the target and multipath echo power.

(6) Figure 12b,k,l consider the RD maps under different SNRs, and the results show that with the SNR increases, the target and multipath become more apparent on the RD maps.

Set B_W = 20M Hz, V_t = [0, 250, 0] m/s, S_z = 1 km, and SNR = 10 dB, and other parameters are the same as the scenario setups in Figure 12. Figure 13 shows the variation in maximum multipath power and maximum target power in the RD maps with target height T_z and sea surface wind speed v_{10}.

As can be seen from Figure 13, with the increase in target height and sea surface wind speed, the maximum multipath echo power decreases. This is due to the reduction in multipath scattering. At the same time, as observed in Figure 13, the changes in sea state have a small impact on the maximum echo of the target, while the maximum target echo increases with the increase in target height. This is due to the decrease in the distance between the target and the radar, resulting in an increase in the target echo.

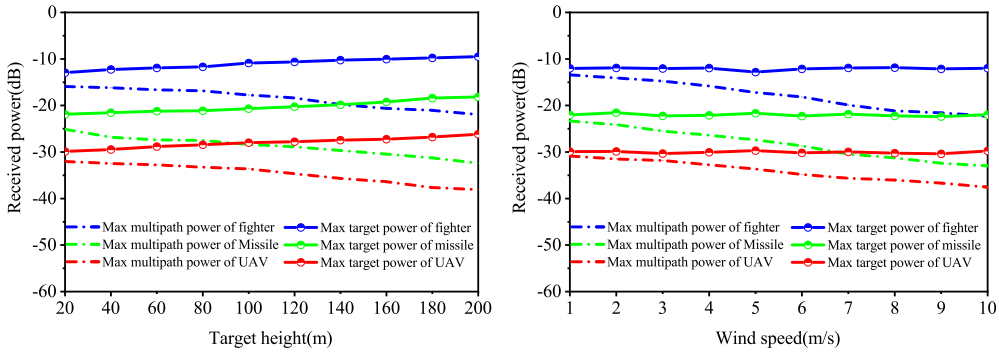


Figure 13. The maximum multipath power versus target height Tz and sea surface wind speed v_{10}. (**a**) The maximum multipath power versus target height with fixed v_{10} = 5 m/s. (**b**) The maximum multipath power versus wind speed with fixed T_z = 50 m.

It should be noted that this conclusion applies to the overall changes in target and multipath in the RD maps. When the velocity of the target, the signal bandwidth of the radar, the SNR, and other parameters change, the target echo and multipath echo may be submerged in the clutter and noise.

Therefore, from the simulations above, there is always a multipath signal around the target echo for typical ultra-low-altitude targets (target height less than 100 m). We define

the target and multipath as the generalized targets in the RD maps and utilize the features of these generalized targets for feature learning by DL-based detectors.

4.3. Analysis of Generalized Target Detection

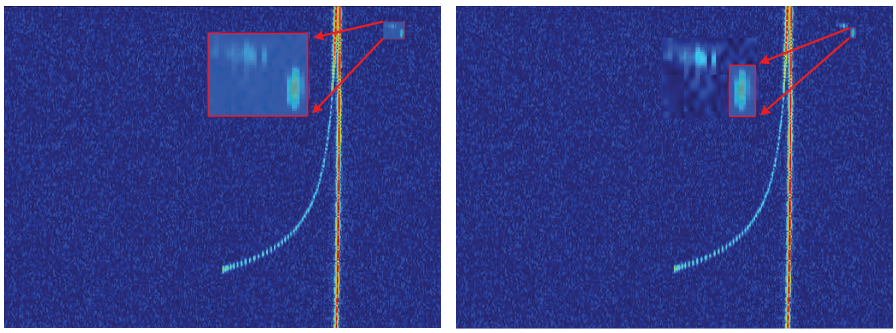
4.3.1. Datasets

Based on the echo generation model in Section 3, the RD maps used for training YOLOv7 and Faster R-CNN are simulated and obtained, with fixed S_p = [0, 0, 300] m, $v_{rx} = v_{rz} = 0$ m/s, $T_x = 0$ m, $f_0 = 10$G Hz, $f_r = 100$k Hz, $K = 512$, $v_{rx} = v_{rz} = 0$ m/s, $v_{tx} = v_{tz} = 0$ m/s, $T_p = 2 \times 10^{-7}$ s, and ε_r = (56.1865, 37.4300). The incidence and reception of the airborne radar are both VV polarization, and the radar uses a two-dimensional array antenna with 64 × 64 elements. The radar main lobe is aligned with the target, and the radar side lobe gain is −15 dB. The target type is randomly selected from PEC missile, PEC fighter, and PEC UAV. The values of other parameters are randomly selected from a specific range, and are shown in Table 2.

Table 2. Simulation parameters for generating the datasets.

Parameter	Symbol	Value Range
Wind speed	v_{10}	[1, 10] m/s
Target y coordinate	T_y	[400, 2000] m
Target z coordinate	T_z	[10, 120] m
Signal bandwidth	B_W	[5, 40] MHz
Target velocity	v_{ty}	[−600, 600] m/s
Radar velocity	v_{ry}	[300, 600] m/s
Noise	SNR	[5, 20] dB

After the RD maps are generated, each RD map is labeled with a target bounding box using labelImg 2 [50] software to create XML tags. As shown in Figure 14, the dataset is constructed by labeling the target and the generalized target for each RD map, respectively. A total of 600 RD maps are obtained, and the dataset is randomly divided into training, validation, and test datasets according to the ratio of 8:1:1.



(**a**) (**b**)

Figure 14. The label diagram of RD maps. (**a**) The proposed method based on the generalized target. (**b**) The conventional method based on the target only.

In this study, the training and testing are implemented on PyTorch 1.10 using NVIDIA GeForce RTX 8000 GPUs (NVIDIA, Santa Clara, CA, USA). The models are trained for 300 epochs, using the Adam optimizer for training, with an initial learning rate of 10^{-4}. The batch size is 16, and the size of the images for the backbone layer after preprocessing the input images is 640 × 640.

4.3.2. Evaluation Metrics and Model Training Results

To evaluate the detection performance of different detectors, the precision, recall, F1 score, and mean average precision (*mAP*) are usually selected as the evaluation metrics [51], and their expressions can be expressed as

$$\text{Precision}: P = \frac{TP}{(TP + FP)} \tag{24}$$

$$\text{Recall}: R = \frac{TP}{(TP + FN)} \tag{25}$$

$$F1\ \text{score} = \frac{P \cdot R}{P + R} \tag{26}$$

$$AP_i = \int_0^1 P_i(R_i) d(R_i) \tag{27}$$

$$mAP = \frac{1}{n} \sum_{i=1}^{n} AP_i \tag{28}$$

where TP, FP, and FN represent true positive samples, false positive samples, and false negative samples, respectively. P and R represent the proportion of true positive examples in the prediction results and in the sample that are correctly predicted, respectively. The $F1$ score is a weighted average of P and R. AP represents the area value under the curve of the P and R metrics. mAP is the average of AP, which represents the overall detection accuracy of the detectors. In this study, the mAP metric is chosen to measure the overall detection performance of YOLOv7 and Faster R-CNN on the two datasets.

As shown in Figure 15, to measure the training degree during the training process, the metrics of training loss and validation loss from all training outcomes using YOLOv7 and Faster R-CNN are aggregated. Due to the difference between the training and validation data, the difference between the value of training loss and validation loss is relatively high in the first 50 epochs. However, the value of the training loss and validation loss gradually decreases as the training epochs increase. The loss values remain almost unchanged after 150 epochs for YOLOv7 and 200 epochs for Faster R-CNN, which indicates that the training of the two detectors achieves the best fit.

To validate the overall detection performance of YOLOv7 and Faster R-CNN, Figure 16 shows the *mAP@0.5* curves. On the whole, the curves illustrate a consistent upward trend in the *mAP* score during the early training epochs. However, they stabilize as the number of training epochs increases. For YOLOv7, the values of *mAP@0.5* are stabilized at around 0.98 by the proposed method and 0.76 by the conventional method. For the faster R-CNN, the values of *mAP@0.5* are stabilized at around 0.58 by the proposed method and 0.48 by the conventional method. Therefore, for both detectors, the detection accuracy of the proposed method is higher than that of the conventional method.

At the same time, it can be seen from Figure 16 that during the initial epochs, the increasing speed of the value of *mAP@0.5* by the proposed method is greater than that by the conventional method. From the above results, it can be concluded that the feature of the generalized target with joint multipath information can be learned more efficiently than just learning the feature of the target by the DL-based detectors. Meanwhile, it can be seen from Figure 16 that the detection performance of YOLOv7 is better than that of Faster R-CNN. Therefore, in the following experiments, the testing is all based on the model trained by YOLOv7, and to compare the detection performance of the proposed method with that of the conventional method, the confidence threshold of the detector is set as 0.2 when testing.

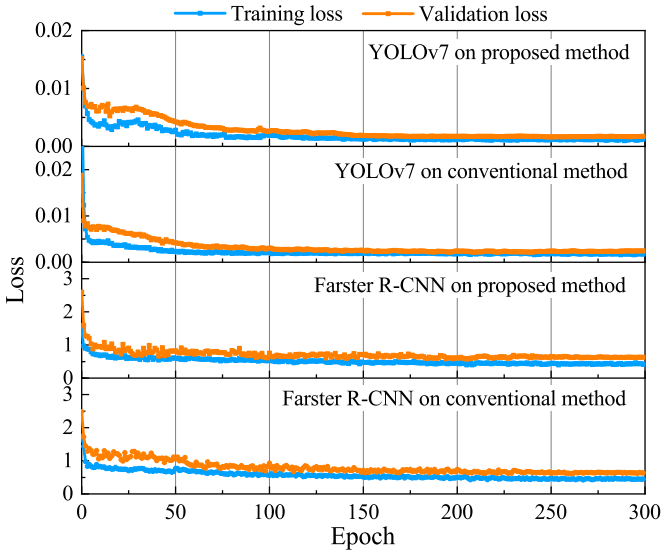


Figure 15. The changes in the value of training loss and validation loss.

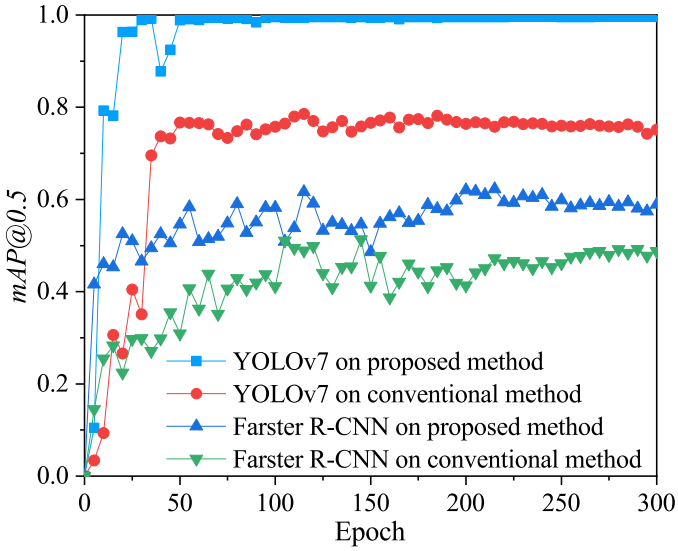


Figure 16. Comparison of the *mAP@0.5* curves.

4.3.3. Testing Results on Simulated Data

Running the trained YOLOv7 on the testing datasets of simulated RD maps, the test results of the same RD maps under different parameters of target, radar, and clutter distribution are shown in Figure 17, where the red circles represent the target is missed or false detection. It shows that under different conditions, such as low target height (Figure 17a,c) and weak target echo power (Figure 17b,d), the confidence scores of the detection results based on generalized target features are higher than those of the conventional method. At the same time, just learning the target feature leads to missed or false detections (Figure 17d) in the RD maps.

Running the trained YOLOv7 on the simulated RD maps of multiple targets, the test results are shown in Figure 18, where the results of two targets in the RD maps are shown in Figure 18a,b, and the results of three targets in the RD maps are shown in Figure 18c,d; the subscripts 1, 2, and 3 in the figure caption denote targets 1, 2, and 3, respectively, from left to right in the RD maps. It can be seen from Figure 18 that although only the features of a single target in RD maps are learned during training, targets can be accurately detected in RD maps by learning the features of generalized targets. However, just learning the target feature leads to missed or false detections, and the confidence scores of the

detection results based on generalized target features are usually higher than those of the conventional method.

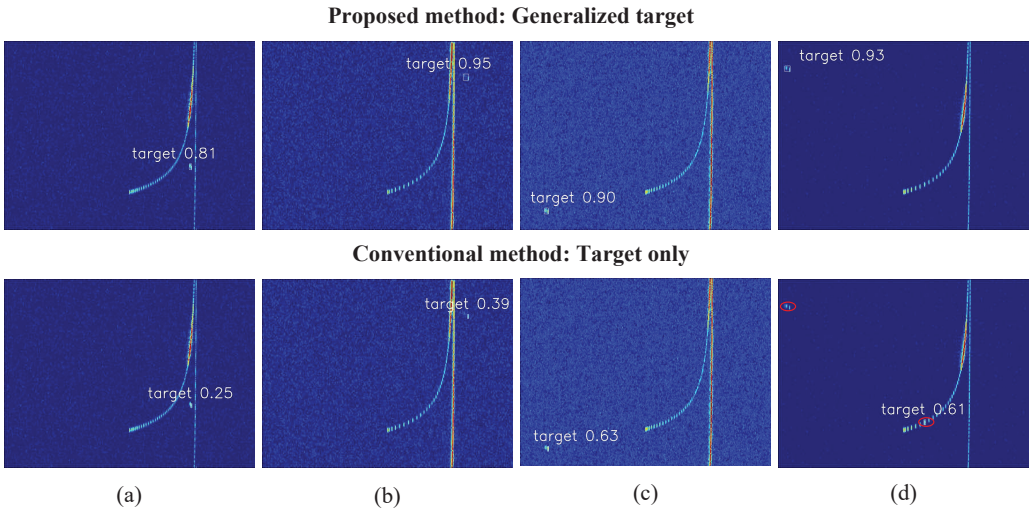


Figure 17. Detection results of the simulated RD maps with a single target. Simulation parameters: (**a**) $v_{10} = 4$ m/s, $T_y = 1978$ m, $T_z = 13$ m, $B_W = 19$ MHz, $v_{ty} = 28$ m/s, $v_{ry} = 395$ m/s, SNR = 12 dB, target type: missile; (**b**) $v_{10} = 6$ m/s, $T_y = 1175$ m, $T_z = 44$ m, $B_W = 10$ MHz, $v_{ty} = -102$ m/s, $v_{ry} = 400$ m/s, SNR = 9 dB, target type: UAV; (**c**) $v_{10} = 2$ m/s, $T_y = 1642$ m, $T_z = 19$ m, $B_W = 15$ MHz, $v_{ty} = -543$ m/s, $v_{ry} = 399$ m/s, SNR = 5 dB, target type: fighter; (**d**) $v_{10} = 3$ m/s, $T_y = 1245$ m, $T_z = 26$ m, $B_W = 10$ MHz, $v_{ty} = -458$ m/s, $v_{ry} = 405$ m/s, SNR = 19 dB, target type: UAV.

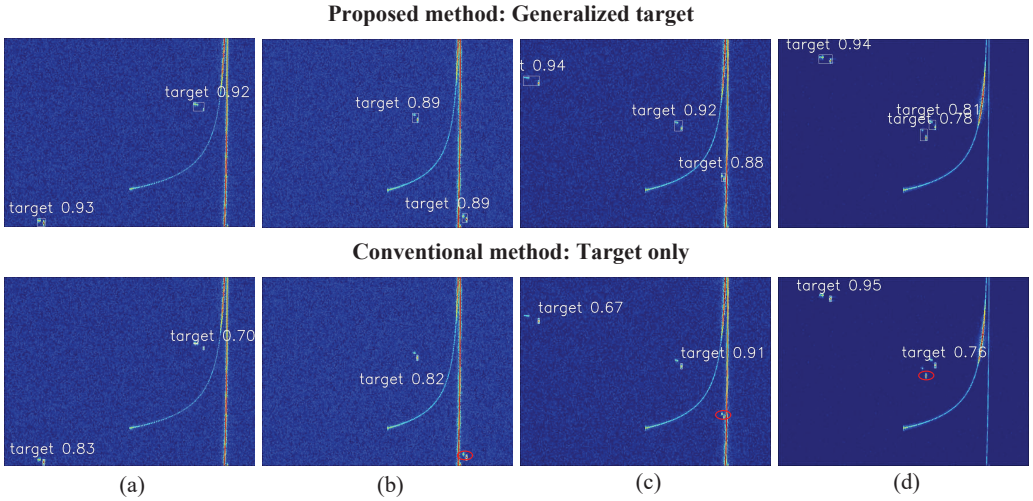


Figure 18. Detection results of simulated RD maps with multiple targets. Simulation parameters: (**a**) $v_{10} = 6$ m/s, $B_W = 38$ MHz, SNR = 8 dB, $v_{ry} = 587$ m/s, $T_{y1} = 1512$ m, $T_{z1} = 47$ m, $v_{ty1} = -426$ m/s, type of target 1: missile, $T_{y2} = 923$ m, $T_{z2} = 60$ m, $v_{ty2} = 117$ m/s, type of target 2: fighter; (**b**) $v_{10} = 4$ m/s, $B_W = 36$ MHz, SNR = 7 dB, $v_{ry} = 437$ m/s, $T_{y1} = 823$ m, $T_{z1} = 51$ m, $v_{ty1} = 244$ m/s, type of target 1: missile, $T_{y2} = 1551$ m, $T_{z2} = 67$ m, $v_{ty2} = -42$ m/s, type of target 2: missile; (**c**) $v_{10} = 5$ m/s, $B_W = 40$ MHz, SNR = 9 dB, $v_{ry} = 494$ m/s, $T_{y1} = 1132$ m, $T_{z1} = 80$ m, $v_{ty1} = -398$ m/s, type of target 1: fighter, $T_{y2} = 1878$ m, $T_{z2} = 67$ m, $v_{ty2} = 21$ m/s, type of target 2: missile, $T_{y3} = 754$ m, $T_{z3} = 55$ m, $v_{ty3} = 259$ m/s, type of target 3: missile; (**d**) $v_{10} = 3$ m/s, $B_W = 40$ MHz, SNR = 20 dB, $v_{ry} = 513$ m/s, $T_{y1} = 1103$ m, $T_{z1} = 62$ m, $v_{ty1} = -582$ m/s, type of target 1: fighter, $T_{y2} = 679$ m, $T_{z2} = 73$ m, $v_{ty2} = 360$ m/s, type of target 2: UAV, $T_{y3} = 763$ m, $T_{z3} = 55$ m, $v_{ty3} = 306$ m/s, type of target 3: missile.

Figure 19 shows the detection results of simulated RD maps with low-speed targets. As shown in Figure 19, when the target velocity is slow, the target echo is submerged in or closed to the clutter, so detecting the target from the interferences is difficult when only learning the target echo features. However, by learning the generalized target features together with the multipath information, it is possible to detect the target even when the target echo is submerged in clutter or close to the clutter region, and the detection results obtained by our proposed method also always have higher confidence scores.

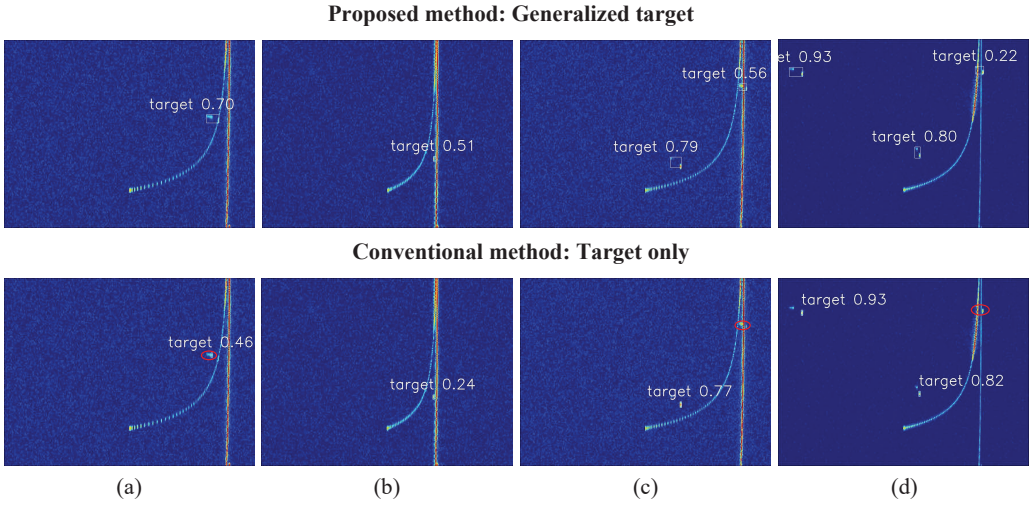


Figure 19. Detection results of simulated RD maps with low-speed targets. Simulation parameters: (**a**) v_{10} = 1 m/s, B_W = 16 MHz, SNR = 8 dB, v_{ry} = 600 m/s, T_y = 817 m, T_z = 44 m, v_{ty} = 20 m/s, type of target 1: missile; (**b**) v_{10} = 3 m/s, B_W = 20 MHz, SNR = 9 dB, v_{ry} = 300 m/s, T_y = 493 m, T_z = 50 m, v_{ty} = −47 m/s, type of target 1: missile; (**c**) v_{10} = 4 m/s, B_W = 22 MHz, SNR = 8 dB, v_{ry} = 590 m/s, T_{y1} = 425 m, T_{z1} = 56 m, v_{ty1} = 314 m/s, type of target 1: missile, T_{y2} = 1182 m, T_{z2} = 40 m, v_{ty2} = −43 m/s, type of target 2: fighter; (**d**) v_{10} = 2 m/s, B_W = 30 MHz, SNR = 18 dB, v_{ry} = 467 m/s, T_{y1} = 1205 m, T_{z1} = 78 m, v_{ty1} = −456 m/s, type of target 1: missile, T_{y2} = 519 m, T_{z2} = 53 m, v_{ty2} = 352 m/s, type of target 2: UAV, T_{y3} = 1216 m, T_{z3} = 78 m, v_{ty3} = −19 m/s, type of target 3: fighter.

4.3.4. Testing Results on Real-Measured Data

We run the trained YOLOv7 on the testing datasets of real-measured RD maps. Due to the limited amounts of real-measured data, only 100 real-measured RD maps of the same target at different moments are included in the test dataset. In addition, due to the significant difference in the maximum clutter distance between the real-measured and simulation RD maps, we only intercept the real-measured data of 1.5 km near the target range unit for testing. Unlike simulated RD maps, there is unintentional jamming in the real-measured data as shown by the vertical line on the RD map in Figure 3.

Figure 20 shows four detection results of the real-measured data. It can be seen from the testing result that even if the real-measured data are not put into the dataset for training, the target can still be accurately detected from the clutter and interference by the proposed method. However, from the testing results of the conventional method, since only the features of the target are learned by the detector, the clutter is detected as the target by mistake.

To measure the overall detection performance of the YOLOv7 on the real-measured data, Figure 21 shows the precision/recall (*PR*) curve on real-measured RD maps. The results show that in the real-measured data, the generalized target features are also more easily learned by the DL-based detector and used for target detection without suppressing interferences.

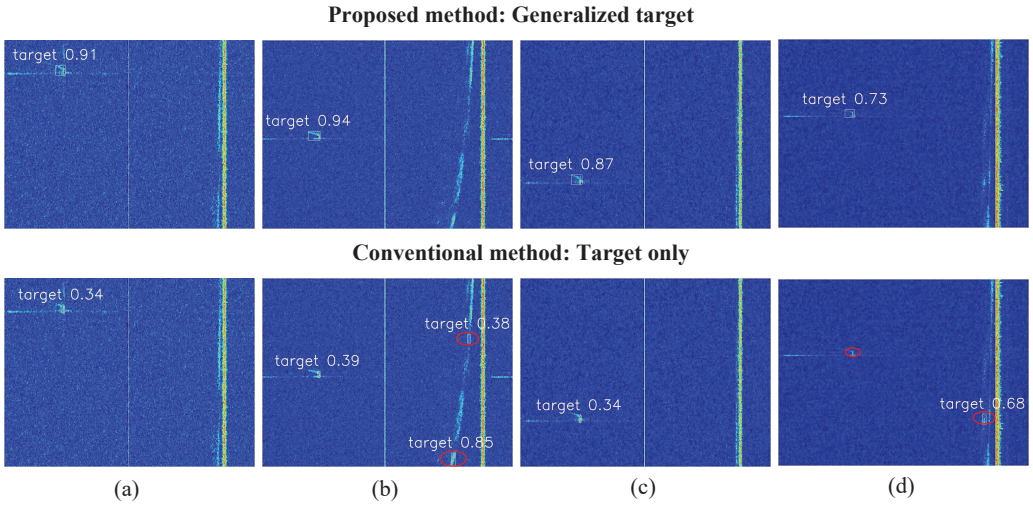


Figure 20. (**a**–**d**) Detection results of real-measured RD maps.

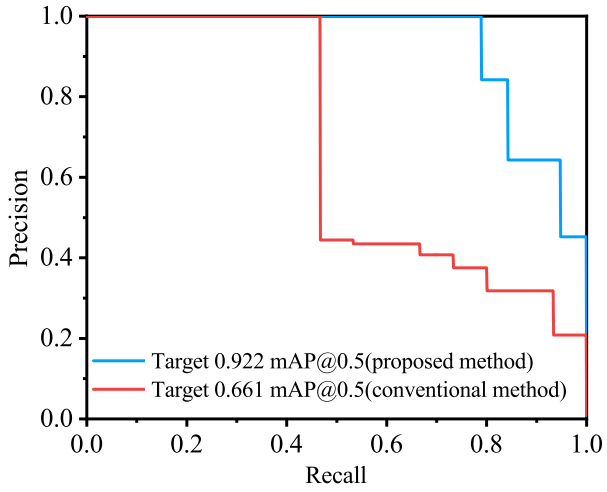


Figure 21. Detection results of real-measured RD maps.

To verify the detection performance of targets in different locations of real-measured RD maps, we re-intercept the 100 RD maps of the real-measured data, in which the target in each RD map is intercepted to be located in different distance ranges as shown in Figure 22, and the average probability that the target is correctly detected at different locations is shown in Figure 23.

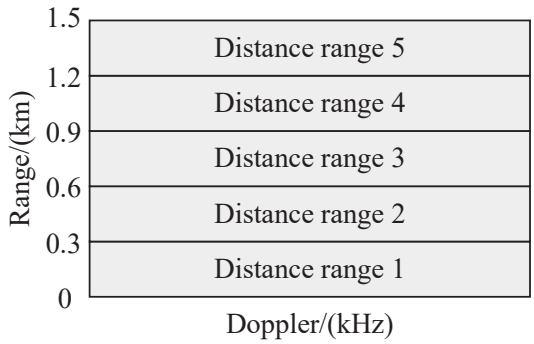


Figure 22. Schematic of different distance ranges.

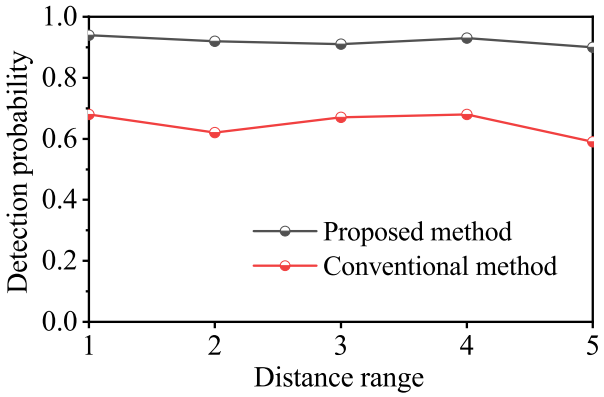


Figure 23. Average probability that the target is correctly detected at different locations.

It can be seen from Figure 23 that the detector has consistent detection performance for targets located at different distance ranges in the real-measured data, which illustrates the effectiveness of detecting real-measured data by intercepting the real-measured data of large clutter distance.

4.3.5. False Alarm Rate

To assess the false alarm rate of the detector, 400 RD maps without target both in the real-measured data and simulated data are obtained, and the changes in the false alarm rate versus the confidence threshold are shown in Figure 24.

It can be seen from Figure 24 that the false alarm rate decreases as the confidence threshold increases, and the overall false alarm rate of the proposed method is lower than that of the conventional method in both simulated and real-measured RD maps, and the false alarm rate of the real-measured RD maps is slightly higher than that of the simulated RD maps. It is worth emphasizing that when the threshold is greater than 0.8, the false alarm rate of the proposed method is 1/400 = 0.0025 in the simulation dataset, and 2/400 = 0.005 in the real-measured dataset. When the threshold is greater than 0.9, the false alarm rates of the proposed method in both datasets are 0/400. Meanwhile, as can be seen from the detection results from Figure 17 to Figure 20, if the confidence threshold is set too high (e.g., more than 0.7) while the false alarm rate can be reduced, most targets will be difficult to detect with the detector using the conventional method.

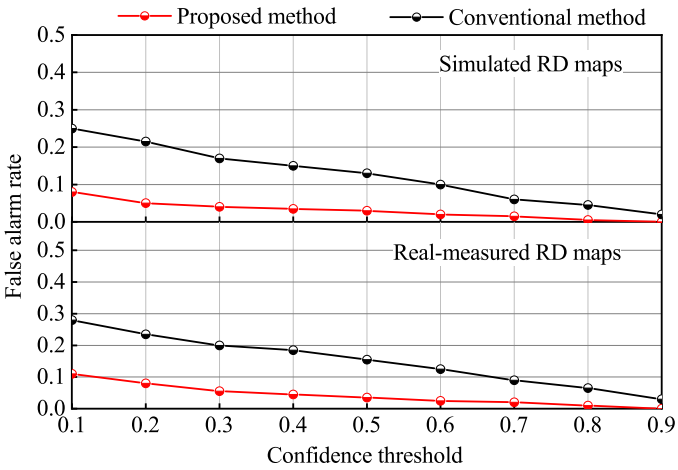


Figure 24. False alarm rate versus different confidence thresholds.

5. Conclusions

In this study, we have developed a novel target detection approach to improve the detection performance of ultra-low-altitude sea-skimming targets by the multipath and

DL-based method. The generalized target is defined after analyzing the image features of the target, multipath, and clutter on the RD maps. Then, sufficient simulated RD maps for DL network training are generated by the proposed scattering-based echo generation model. At last, the targets are detected based on their distinguishable generalized features and the DL techniques without suppressing the interferences. The detection results show the high performance of the proposed method on both simulated and real-measured data.

The limitation of the proposed method is that both the target and multipath are detected simultaneously. In other words, the bounding box includes both the target and multipath. Hence, compared to the bounding box including target only, further processing steps are required to accurately extract the target parameters, such as its velocity and range. In addition, the impact of sea swell on the clutter is not considered; the corresponding surface model, scattering model, and echo generation model need to be further established to more accurately mimic the echo characteristics of the sea. Additionally, we directly use existing DL networks for target detection, without structural adjustments or optimizations. To further improve the detection performance, designing new DL networks to better exploit the target features is on the list of our future work. At last, expanding the dataset by incorporating micro-motion features of targets will also be studied.

Author Contributions: Conceptualization, Z.W.; Formal analysis, W.F.; Funding acquisition, W.F., T.W. and X.C.; Investigation, B.Z., T.W. and C.Q.; Project administration, X.Z.; Resources, X.Z. and W.F.; Software, Z.W.; Supervision, C.Q.; Validation, Z.W. and B.Z.; Writing—original draft, Z.W.; writing—review and editing, X.C. All authors have read and agreed to the published version of the manuscript.

Funding: This work was supported in part by the Youth Talent Lifting Project of the China Association for Science and Technology under Grant 2021-JCJQ-QT-018; in part by the National Natural Science Foundation of China under Grant 62201611, Grant 62301597, and Grant 62301598; in part by the Youth Innovation Team of Shaanxi Universities; in part by the Natural Science Foundation of Shannxi Province under Grant 2023-JC-QN-0647 and Grant 2023-JC-YB-488.

Data Availability Statement: The original contributions presented in the study are included in the article, further inquiries can be directed to the corresponding author.

Conflicts of Interest: The authors declare no conflicts of interest.

Appendix A

Appendix A.1 Calculation Scheme of the NRCS of the Ocean Rough Surface

The following derivations are elucidated to obtain (10), the NRCS of the ocean rough surface.

As shown in Figure A1, the ocean surface contains large- and small-scale parts. The small-scale contour distribution corresponds to the high-frequency part of the Elfouhaily spectrum, and the scattering coefficient is calculated using the small perturbation method (SPM). The Kirchhoff approximation method (KAM) is used for the scattering calculation for the large-scale part. The total scattering can be considered a combination of the two parts.

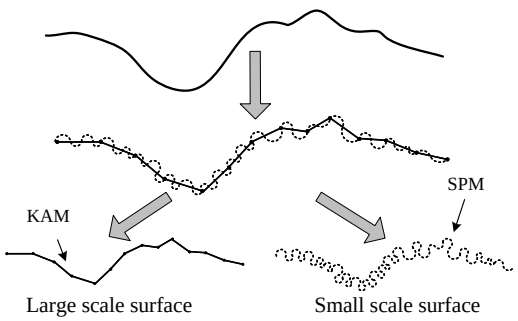


Figure A1. The two-scale model.

The scattering field of each facet on the ocean surface can be obtained as [52]

$$\boldsymbol{E}^{s}_{facet}(\hat{\boldsymbol{k}}_{\mathrm{i}}, \hat{\boldsymbol{k}}_{\mathrm{s}}) = 2\pi \frac{e^{\mathrm{j}kR_0}}{\mathrm{j}R_{\mathrm{o}}} S_{hv}(\hat{\boldsymbol{k}}_{\mathrm{i}}, \hat{\boldsymbol{k}}_{\mathrm{s}}) \tag{A1}$$

where $\hat{\boldsymbol{k}}_{\mathrm{i}}$ and $\hat{\boldsymbol{k}}_{\mathrm{s}}$ represent the unit vector along the incident and scattering directions, k is the EM wave number, R_0 is the distance from the facet centers to the receiver, j represents the imaginary unit, and the subscripts v and h represent the vertical and horizontal polarizations. S_{hv} is the scattering amplitude [53] and can be expressed as

$$S_{hv}(\hat{\boldsymbol{k}}_{\mathrm{i}}, \hat{\boldsymbol{k}}_{\mathrm{s}}) = \frac{k^2(1-\varepsilon)}{8\pi^2} F_{hv} \iint \zeta(r) e^{-\mathrm{j}k(\hat{k}_{\mathrm{s}} - \hat{k}_{\mathrm{i}})\cdot r} dr \tag{A2}$$

where $\zeta(r)$ represents the small ripples on each facet, ε represents the relative permittivity, and F_{hv} is the polarimetric coefficient. The scattering of the ocean surface is generally expressed in the form of scattering coefficients. Based on (A1) and the definition of scattering coefficient [54], the scattering coefficient of each small facet can be expressed as

$$\sigma^{\mathrm{SPM}}_{hv}(\hat{\boldsymbol{k}}_i, \hat{\boldsymbol{k}}_{\mathrm{s}}) = \pi k^4 |\varepsilon - 1|^2 |F_{hv}|^2 \boldsymbol{S}_{\zeta}(\boldsymbol{q}_{\mathrm{l}}) \tag{A3}$$

where $\boldsymbol{S}_{\zeta}(\boldsymbol{q}_{\mathrm{l}})$ represents the high-frequency part of the Elfouhaily spectrum. The scattering of small-scale facets is modulated by large-scale facets. Based on the KAM [55], the scattering coefficient of a large-scale facet can be expressed as

$$\sigma^{\mathrm{KAM}}_{hv}(\hat{\boldsymbol{k}}_{\mathrm{i}}, \hat{\boldsymbol{k}}_{\mathrm{s}}) = \frac{\pi (k\mathbf{q}|\Gamma_{hv}|)^2}{|q_z|^4} prob(\cdot) \tag{A4}$$

where $\mathbf{q} = k(\hat{k}_s - \hat{k}_i) = q_x\hat{x} + q_y\hat{y} + q_z\hat{z}$, $\hat{x}$, $\hat{y}$ and $\hat{z}$ are the unit direction vectors of the global coordinate system, respectively, $|\Gamma_{hv}|$ is the polarimetric parameter depending on the incident and scattering vector $(\hat{\boldsymbol{k}}_{\mathrm{i}}, \hat{\boldsymbol{k}}_{\mathrm{s}})$ and the Fresnel coefficients [56], and prob$(\cdot)$ represents the probability density function of large-scale facets, which is defined in [57].

Finally, the NRCS of the total ocean rough surface can be expressed as

$$\sigma^{total}_{hv}\left(\hat{\boldsymbol{k}}_{\mathrm{i}}, \hat{\boldsymbol{k}}_{\mathrm{s}}\right) = \frac{1}{A'} \cdot \sum_{n=1}^{N'} \left\{ \left[\sigma^{\mathrm{KAM}}_{hv}(\hat{\boldsymbol{k}}_{\mathrm{i}}, \hat{\boldsymbol{k}}_{\mathrm{s}})_n + \sigma^{\mathrm{SPM}}_{hv}(\hat{\boldsymbol{k}}_{\mathrm{i}}, \hat{\boldsymbol{k}}_{\mathrm{s}})_n \right] \Delta S_n \right\} \tag{A5}$$

Appendix A.2 Calculation Scheme of the i-th Reflection on a Triangular Facet

The following derivations are elucidated to show the i-th reflection on a triangular facet based on the GO method.

Figure A2 shows the i-th reflection of point P_i on triangular facet S_n, where θ_i and θ_r are the incidence angle and reflection angle, respectively, $\hat{\boldsymbol{R}}_i$ and $\hat{\boldsymbol{R}}_r$ are unit vectors of the incident direction and reflection direction, respectively, and $\boldsymbol{n}_i$ represents the unit normal direction of the triangle facet element. According to the Snell's reflection theorem [58], θ_r and $\hat{\boldsymbol{R}}_r$ can be obtained as

$$\theta_r = \theta_i \tag{A6}$$

$$\hat{\boldsymbol{R}}_r = \hat{\boldsymbol{R}}_i - 2(\hat{\boldsymbol{R}}_i \cdot \hat{\boldsymbol{n}}_i)\hat{\boldsymbol{n}}_i \tag{A7}$$

The reflected field $\hat{\boldsymbol{E}}_r(\hat{r}_{p_i})$ can be obtained from the incident field. Set the incident field vector at point P_i as $\hat{\boldsymbol{E}}_i(\hat{r}_{\boldsymbol{p}_i}) = E_v\hat{\boldsymbol{e}}_v + E_h\hat{\boldsymbol{e}}_h$, and the reflected field can be obtained as

$$\hat{\boldsymbol{E}}_r(\hat{r}_{p_i}) = (DF)_i(R_vE_v\hat{\boldsymbol{e}}_v + R_hE_h\hat{\boldsymbol{e}}_h) \tag{A8}$$

where the subscripts v and h represent the vertical and horizontal polarization, respectively, $\hat{\boldsymbol{e}}_{v/h}$ is the unit vector of the polarization direction, $E_{v/h}$ represents the amplitude of the

field in the horizontal or vertical polarization direction, and $(DF)_i$ represents the diffusion coefficient of the ray tube at point P_i. As the ocean surface and target are divided into triangular facets in this paper, the corresponding diffusion factor $(DF)_i = 1$. R_v and R_h are the facet surface Snell reflection coefficients under vertical and horizontal polarization. R_v and R_h can be expressed as

$$R_v = \frac{\cos\theta_i - \sqrt{\mu_r\varepsilon_r - \sin^2\theta_i}}{\cos\theta_i + \sqrt{\mu_r\varepsilon_r - \sin^2\theta_i}} \tag{A9}$$

$$R_h = \frac{\varepsilon_r\cos\theta_i - \sqrt{\mu_r\varepsilon_r - \sin^2\theta_i}}{\varepsilon_r\cos\theta_i + \sqrt{\mu_r\varepsilon_r - \sin^2\theta_i}} \tag{A10}$$

where ε_r and μ_r represent the relative permittivity and the relative permeability, respectively. In particular, for the perfect electric conductor of target facets, $R_v = -1$ and $R_h = 1$.

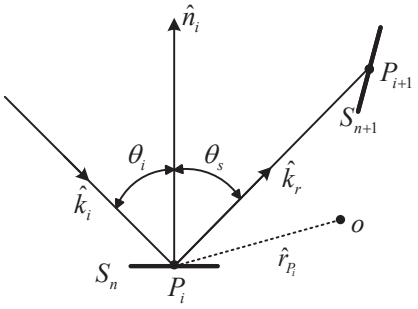


Figure A2. The i-th reflection on the triangular facet S_n.

References

1. Chen, X.; Liu, K.; Zhang, Z. A PointNet-Based CFAR Detection Method for Radar Target Detection in Sea Clutter. *IEEE Geosci. Remote Sens. Lett.* **2024**, *21*, 3502305. [CrossRef]
2. Wang, C.; Tian, J.; Cao, J.; Wang, X. Deep Learning-Based UAV Detection in Pulse-Doppler Radar. *IEEE Trans. Geosci. Remote Sens.* **2022**, *60*, 1–12. [CrossRef]
3. Qi, Q.; Xie, J.; Zhang, H.; Liu, W.; Feng, W.; Zheng, G. Optimizing low-grazing angle detection for maneuvering targets in cognitive MIMO radar networks: A shapley value approach. *IEEE Trans. Veh. Technol.* 2024, *early access*.
4. Skolnik, M.I. *Introduction to RADAR Systems*; McGraw-Hill: New York, NY, USA, 1990; pp. 35–67.
5. Van Veen, B.D. Buckley, K.M. Beamforming: A versatile approach to spatial filtering. *IEEE Aerosp. Electron. Syst. Mag.* **1988**, *5*, 4–24.
6. Melvin, W.L. A STAP overview. *IEEE ASSP Mag.* **2004**, *19*, 19–354. [CrossRef]
7. Duan, K.; Xu, H.; Yuan, H.; Xie, H.; Wang, Y. Reduced-DOF three-dimensional STAP via subarray synthesis for nonsidelooking planar array airborne radar. *IEEE Trans. Aerosp. Electron. Syst.* **2020**, *56*, 3311–3325. [CrossRef]
8. Huang, P.; Zou, Z.; Xia, X.G.; Liu, X.; Liao, G. A novel dimension-reduced space–time adaptive processing algorithm for spaceborne multichannel surveillance radar systems based on spatial-temporal 2-D sliding window. *IEEE Trans. Geosci. Remote Sens.* **2022**, *60*, 5109721. [CrossRef]
9. He, X.; Liao, G.; Duan, K.; Zhu, S. Range ambiguous clutter suppression for the SAR-GMTI system based on extended azimuth phase coding. *IEEE Trans. Geosci. Remote Sens.* **2020**, *58*, 8147–8162. [CrossRef]
10. Deng, H.; Geng, Z.; Himed, B. Radar Target Detection Using Target Features and Artificial Intelligence. In Proceedings of the 2018 International Conference on Radar (RADAR), Brisbane, QLD, Australia, 27–31 August 2018; pp. 1–4.
11. Geng, Z.; Deng, H.; Himed, B. Ground Moving Target Detection Using Beam-Doppler Image Feature Recognition. *IEEE Trans. Aerosp. Electron. Syst.* **2018**, *54*, 2329–2341. [CrossRef]
12. Tm, D.; Vermag, R.; Rajesh, R.; Varughes, S. Single Shot Radar Target Detection and Localization using Deep Neural Network. In Proceedings of the 2022 IEEE International Conference on Electronics, Computing and Communication Technologies (CONECCT), Bangalore, India, 8–10 July 2022; pp. 1–9.
13. Jokanović, B.; Amin, M. Fall Detection Using Deep Learning in Range-Doppler Radar. *IEEE Trans. Aerosp. Electron. Syst.* **2018**, *54*, 180–189. [CrossRef]
14. Kim, Y.; Moon, T. Human Detection and Activity Classification Based on Micro-Doppler Signatures Using Deep Convolutional Neural Networks. *IEEE Geosci. Remote Sens. Lett.* **2016**, *13*, 8–12. [CrossRef]

15. Li, J.; Xu, C.; Su, H.; Gao, L.; Wang, T. Deep Learning for SAR Ship Detection: Past, Present and Future. *Remote Sens.* **2022**, *14*, 2712. [CrossRef]
16. Gu, G.F.; Zhou, W.X. Detrending moving average algorithm for multifractals. *Phys. Rev. E* **2010**, *82*, 011136. [CrossRef]
17. Xiong, G.; Wang, F.; Zhu, L.; Li, J.; Yu, W. SAR target detection in complex scene based on 2-D singularity power spectrum analysis. *IEEE Trans. Geosci. Remote Sens.* **2019**, *57*, 9993–10003. [CrossRef]
18. Cui, Z.; Wang, X.; Liu, N.; Cao, Z.; Yang, J. Ship detection in large-scale SAR images via spatial shuffle-group enhance attention. *IEEE Trans. Geosci. Remote Sens.* **2021**, *59*, 379–391. [CrossRef]
19. Qin, X.; Zhou, S.; Zou, H.; Gao, G. A CFAR detection algorithm for generalized gamma distributed background in high-resolution SAR images. *IEEE Geosci. Remote Sens. Lett.* **2012**, *10*, 806–810.
20. Yang, Y.; Feng, D.j.; Wang, X.S.; Xiao, S.P. Effects of K distributed sea clutter and multipath on radar detection of low altitude sea surface targets. *IET Radar Sonar Navig.* **2014**, *8*, 757–766. [CrossRef]
21. Sinha, A.; Bar-Shalom, Y.; Blair, W.D.; Kirubarajan, T. Radar measurement extraction in the presence of sea-surface multipath. *IEEE Trans. Aerosp. Electron. Syst.* **2003**, *39*, 550–567. [CrossRef]
22. Xu, Z.; Fan, C.; Huang, X. MIMO Radar Waveform Design for Multipath Exploitation. *IEEE Trans. Signal Process.* **2021**, *69*, 5359–5371. [CrossRef]
23. Trizna, D.B. A model for Brewster angle damping and multipath effects on the microwave radar sea echo at low grazing angles. *IEEE Trans. Geosci. Remote Sens.* **1997**, *35*, 1232–1244. [CrossRef]
24. Smit, J.C.; Cilliers, J.E.; Baker, C.J.; Hanekom, J.J. X-Band high range resolution radar measurements of sea surface forward scatter at low grazing angles. In Proceedings of the 2008 IEEE Radar Conference, Rome, Italy, 26–30 May 2008; pp. 1–4.
25. Al-Ardi, E.M.; Shubair, R.M.; Al-Mualla, M.E. Computationally efficient high-resolution DOA estimation in multipath environment. *Electron. Lett.* **2004**, *40*, 908–910. [CrossRef]
26. Aubry, A.; De Maio, A.; Foglia, G.; Orlando, D. Diffuse Multipath Exploitation for Adaptive Radar Detection. *IEEE Trans. Signal Process.* **2015**, *63*, 1268–1281. [CrossRef]
27. Satyabrata, S.; Hurtado, M.; Nehorai, A. Adaptive OFDM Radar for Detecting a Moving Target in Urban Scenarios. In Proceedings of the 2009 International Waveform Diversity and Design Conference, Kissimmee, FL, USA, 8–13 February 2009; pp. 268–272.
28. Sen, S.; Nehorai, A. Adaptive OFDM Radar for Target Detection in Multipath Scenarios. *IEEE Trans. Signal Process.* **2011**, *59*, 78–90. [CrossRef]
29. Guendel, R.G.; Kruse, N.C.; Fioranelli, F.; Yarovoy, A. Multipath Exploitation for Human Activity Recognition Using a Radar Network. *IEEE Trans. Geosci. Remote Sens.* **2024**, *62*, 5103013. [CrossRef]
30. Setlur, P.; Amin, M.; Ahmad, F. Multipath Model and Exploitation in Through-the-Wall and Urban Radar Sensing. *IEEE Trans. Geosci. Remote Sens.* **2011**, *49*, 4021–4034. [CrossRef]
31. Wu, Q.; Lai, Z.; Amin, M.G. Through-the-Wall Radar Imaging Based on Bayesian Compressive Sensing Exploiting Multipath and Target Structure. *IEEE Trans. Comput. Imaging* **2021**, *7*, 422–435. [CrossRef]
32. Karlsson, A.; Jansson, M.; Hämäläinen, M. Low-Angle Target Tracking in Sea Surface Multipath Using Convolutional Neural Networks. *IEEE Trans. Aerosp. Electron. Syst.* **2023**, *59*, 6813–6831. [CrossRef]
33. Li, X.; Xu, X. A Statistical Model for Correlated K-distributed Sea Clutter. In Proceedings of the 2008 Congress on Image and Signal Processing, Sanya, Hainan, China, 27–30 May 2008; pp. 408–412.
34. Gregers-Hansen, V.; Mital, R. An Improved Empirical Model for Radar Sea Clutter Reflectivity. *IEEE Trans. Aerosp. Electron. Syst.* **2012**, *48*, 3512–3524. [CrossRef]
35. Xin, Z.; Liao, G.; Yang, Z.; Zhang, Y.; Dang, H. A Deterministic Sea-Clutter Space–Time Model Based on Physical Sea Surface. *IEEE Trans. Geosci. Remote Sens.* **2016**, *54*, 6659–6673. [CrossRef]
36. Miret, D.; Soriano, G.; Nouguier, F.; Forget, P.; Saillard, M.; Guérin, C.A. Sea Surface Microwave Scattering at Extreme Grazing Angle: Numerical Investigation of the Doppler Shift. *IEEE Trans. Aerosp. Electron. Syst.* **2014**, *52*, 7120–7129. [CrossRef]
37. Li, D.; Zhao, Z.; Zhao, Y.; Huang, Y.; Liu, Q.H. An Improved Facet-Based Two-scale model for Electromagnetic Scattering from Sea Surface and SAR Imaging. In Proceedings of the 2019 IEEE Radar Conference (RadarConf), Boston, MA, USA, 22–26 April 2019; pp. 1–4.
38. Wang, W.Q.; Wang, L.Y.; Li, X.Z.; Zhang, M. Simulation of a Wideband Radar Echo of a Target on a Dynamic Sea Surface. *Remote Sens.* **2021**, *13*, 3186. [CrossRef]
39. Wangs, J.; Guo, L.; Wei, Y. Chai, S. Application of the Improved SBR-TSM Based on MPI to EM Scattering from Multiple Targets Above a 3-D Rough Sea Surface. *IEEE Antennas Wirel. Propag. Lett.* **2022**, *21*, 411–415. [CrossRef]
40. Wang, C.Y.; Bochkovskiy, A.; Liao, H.Y.M. YOLOv7: Trainable Bag-of-Freebies Sets New State-of-the-Art for Real-Time Object Detectors. In Proceedings of the IEEE/CVF Conference on Computer Vision and Pattern Recognition (CVPR), Vancouver, BC, Canada, 17–24 June 2023; pp. 7464–7475.
41. Ren, S.; He, K.; Girshick, R.; Sun, J. Faster R-CNN: Towards Real-Time Object Detection with Region Proposal Networks. *IEEE Trans. Pattern Anal. Mach. Intell.* **2017**, *3*, 1137–1149. [CrossRef] [PubMed]
42. Liu, S.; Qi, L.; Qin, H.; Shi, J.; Jia, J. Path Aggregation Network for Instance Segmentation. In Proceedings of the 2018 IEEE/CVF Conference on Computer Vision and Pattern Recognition, Salt Lake City, UT, USA, 18–23 June 2018; pp. 8759–8768.
43. Tsang, L. *Scattering of Electromagnetic Waves: Numerical Simulations*; Wiley Interscience: New York, NY, USA, 2001.

44. Tsang, L.; Kong, j.A.; Ding, K.H. *One-Dimensional Random Rough Surface Scattering*; John Wiley and Sons, Inc.: Hoboken, NJ, USA, 2000; pp. 389–417.
45. Zhang, M.; Chen, H.; Yin, H.C. Facet-Based Investigation on EM Scattering from Electrically Large Sea Surface with Two-Scale Profiles: Theoretical Model *IEEE Trans. Geosci. Remote Sens.* **2011**, *49*, 1967–1975. [CrossRef]
46. Schleher, D.C. *MTI and Pulsed Doppler Radar*; Artech House: Norwood, MA, USA, 1999; pp. 171–224.
47. Ling, H.; Chou, R.C.; Lee, S.W. Shooting and bouncing rays: Calculating the RCS of an arbitrarily shaped cavity. *IEEE Trans. Antennas Propag.* **1989**, *37*, 194–205. [CrossRef]
48. Gordon, W.B. High frequency approximations to the physical optics scattering integral. *IEEE Trans. Antennas Propag.* **1994**, *42*, 427–432. [CrossRef]
49. Kane, Y. Numerical solution of initial boundary value problems involving maxwell's equations in isotropic media. *IEEE Trans. Antennas Propag.* **1966**, *14*, 302–307. [CrossRef]
50. Chinakook. LabelImg2. Github. 2018. Available online: https://github.com/chinakook/labelImg2 (accessed on 10 May 2024).
51. Wang, R.; Liang, F.; Mou, X.; Chen, L.; Yu, X.; Peng, Z.; Chen, H. Development of an improved yolov7-based model for detecting defects on strip steel surfaces. *Coatings* **2023**, *13*, 536. [CrossRef]
52. Fuks, I.M. Wave diffraction by a rough boundary of an arbitrary plane-layered medium. *IEEE Trans. Antennas Propag.* **2001**, *49*, 630–639. [CrossRef]
53. Wei, Y.; Guo, L.; Li, J. Numerical Simulation and Analysis of the Spiky Sea Clutter from the Sea Surface With Breaking Waves. *IEEE Trans. Antennas Propag.* **2015**, *63*, 4983–4994. [CrossRef]
54. Ogilvy, J.A. Wave scattering from rough surfaces. *Rep. Prog. Phys.* **1987**, *50*, 1553. [CrossRef]
55. Arnold-Bos, A.; Khenchaf, A.; Martin, A. Bistatic Radar Imaging of the Marine Environment—Part I: Theoretical Background. *IEEE Trans. Geosci. Remote Sens.* **2007**, *45*, 3372–3383. [CrossRef]
56. Ulaby, F.T.; Moore, R.K.; Fung, A.K. *Microwave Remote Sensing: Active and Passive*; Artech House: Norwood, MA, USA, 1986.
57. Cox, C.; Munk, W. Statistics of the sea surface derived from sun glitter. *J. Mar. Res.* **1954**, *13*, 198–227.
58. Kim, H.; Ling, H. Electromagnetic scattering from an inhomogeneous object by ray tracing. *IEEE Trans. Antennas Propag.* **1992**, *40*, 517–525. [CrossRef]

Disclaimer/Publisher's Note: The statements, opinions and data contained in all publications are solely those of the individual author(s) and contributor(s) and not of MDPI and/or the editor(s). MDPI and/or the editor(s) disclaim responsibility for any injury to people or property resulting from any ideas, methods, instructions or products referred to in the content.